Journal of the American Ceramic Society

RESEARCH ARTICLE OPEN ACCESS

The Stability of Gyrolite and Influence of Fe(III)

Serena Mingione[1,2] | Egle Bobinaite[3] | Tadas Dambrauskas[3] | Frank Winnefeld[1] | Barbara Lothenbach[1,2,4]

[1]Empa, Swiss Federal Laboratories for Materials Science and Technology, Laboratory For Concrete & Asphalt, Dübendorf, Switzerland | [2]Institute of Geological Sciences, University of Bern, Bern, Switzerland | [3]Department of Silicate Technology, Kaunas University of Technology, Kaunas, Lithuania | [4]Department of Structural Engineering, NTNU, Trondheim, Norway

Correspondence: Serena Mingione (serena.mingione@empa.ch)

Received: 24 September 2025 | **Revised:** 19 December 2025 | **Accepted:** 26 February 2026

Keywords: calcium silicate hydrate | gyrolite | hydroandradite | solubility product | thermodynamic

ABSTRACT

Gyrolite ($Ca_4Si_6O_{15}(OH)_2{\cdot}4H_2O$) is a crystalline calcium silicate hydrate which forms hydrothermally and is primarily used as an adsorbent for wastewater treatment. The stability of gyrolite is poorly understood, as well as the potential impact of Fe, which can be present as an impurity in the raw materials used. This study investigates the effect of Fe(III) on the formation of gyrolite at 200°C. The presence of Fe(III) during synthesis leads to the formation of hydroandradite, amorphous silica, a poorly crystalline calcium silicate hydrate with $Ca/Si = 0.4$, and less gyrolite. No or very small uptake of Fe(III) in the gyrolite structure was observed. The solubility of gyrolite in the absence and presence of Fe(III) was determined through dissolution experiments at 20°C to 80°C. The results show that gyrolite has a higher stability than previously reported, suggesting it may be a long-term stable phase together with xonotlite at molar Ca/Si ratios < 1.0.

1 | Introduction

Calcium silicate hydrates (C-S-H) can, besides their application in construction materials, be used for water purification from heavy metals and radionuclides due to their high ability to adsorb various ions [1–5]. Depending on temperature, the molar ratio of Ca/Si, and reaction time, different amorphous and crystalline calcium silicate hydrates can form [6–9]. Recently, among the various types of calcium silicate hydrates used as adsorbents for wastewater recovery, attention has shifted toward gyrolite ($Ca_4Si_6O_{15}(OH)_2{\cdot}4H_2O$) [10]. Gyrolite is a crystalline calcium silicate hydrate that forms under hydrothermal conditions. First discovered as a natural mineral in Skye, Scotland, by Anderson [11], gyrolite commonly forms through ion exchange processes in volcanic and basaltic rocks [12, 13].

The crystal structure of gyrolite was first described by Mackay and Taylor [14], who discovered that gyrolite is characterized by a hexagonal unit cell. Gyrolite belongs to the phyllosilicate group, which consists of stacked silicate layers (denoted as S_1 and S_2 in Figure 1) and calcium layers (denoted as O) [15]. Merlino [16] showed that calcium is octahedrally coordinated, and that the calcium layers have a composition of $[Ca_7O_{10}(OH)_4]^{4-}$. These Ca layers are connected on both sides to two different tetrahedral silicate layers: S_1 and S_2, which both have a composition of $[Si_8O_{20}]^{8-}$. They consist of silica tetrahedra, each connected to three other silica tetrahedra by bridging oxygen atoms (Q^3 silicate), forming six-membered rings (Figure 1). The S_1 layer contains both six-membered rings, where (i) the silicate tetrahedra alternatingly point up and down, and (ii) three tetrahedra facing up are connected to three tetrahedra facing down. The S_2 layers consist of rings where most tetrahedra face downward, connected by upward-facing tetrahedra. Those layers are connected by an interlayer labeled X, in a $S_1OS_2XS_2OS_1$ sequence. The interlayer X also contains octahedrally coordinated cations. In synthesized pure gyrolite, the interlayer X typically contains water molecules and Ca-octahedra [17]. In natural gyrolite, however, the presence of one Na and two Ca ions have been

https://doi.org/10.1111/jace.70634

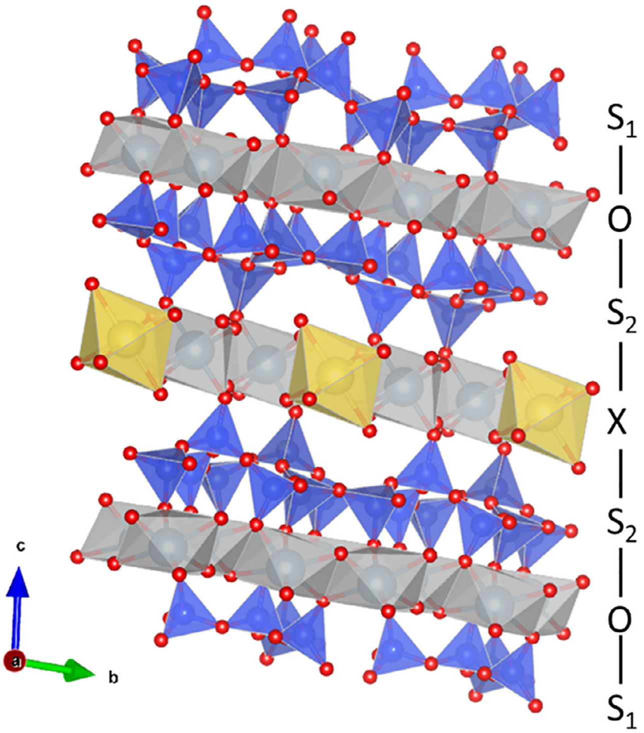

FIGURE 1 | Gyrolite structure visualized by VESTA [19] based on the structural data from Merlino [16]. Gray polyhedra represent 6-fold coordinated calcium in the CaO layer (O layer) and in the interlayer X, which also can contain alkalis such as sodium (yellow octahedra). Blue tetrahedra represent the $[Si_6O_{18}]_{12}$-rings.

found which can lead to a molar ratio of Ca/Si = 0.5–0.66 [16, 18].

Gyrolite has been observed to have a relatively high capacity to sorb various cations under different conditions as the calcium and alkali cations in its interlayer can be exchanged: gyrolite-Ca^0 + $2/xMe^{x+}$ ↔ gyrolite-$2/xMe^0$ + Ca^{2+} [10, 20–24]. Thus, gyrolite can bind various alkali cations such as Na^+, K^+, or Cs^+ in its interlayer [21, 24]. Gyrolite can also take up various heavy metals such as Cu(II), Zn(II), Cd(II), Ni(II), Pb(II), and Fe(III), with a preference for Fe(III) [10], depending on the pH [20, 22, 23, 25]. Zadavicute et al. [26] demonstrated that gyrolite can adsorb up to 98 wt.% of the total added Fe^{3+} (corresponding to 0.3 mol Fe^{3+}/mol of gyrolite) and 40 wt.% of the total added Ni^{2+} (corresponding to 0.11 mol Ni^{2+}/mol of gyrolite) under acidic conditions, releasing Ca^{2+} without altering the crystal structure of gyrolite.

Only a few studies in the literature report thermodynamic properties of pure gyrolite, most of them are estimated data based on the observed stability field of gyrolite [6, 9, 27], which is challenging as various metastable phases can form and persist in experiments, which are thermodynamically not stable in the long-term. Only Dickson et al. [28, 29] reported solubility data at 25°C, 55°C, and 85°C (see Table 1) measured from undersaturation using natural gyrolite from India, without reporting its actual composition or which impurities might have been present. They reported measured pH values, Ca and Si concentrations and calculated based on that very diverging solubility products between $10^{-39.6}$ and $10^{-40.9}$ (if referred to Ca^{2+}, $HSiO_3^-$, OH^-, and H_2O). Recalculations here based on the total concentrations and pH values reported by [28] resulted in solubility products between $10^{-41.2}$ and $10^{-51.1}$ as detailed in Table 1. Babushkin et al. [27], Blanc et al. [9] and Hirsch et al. [6] estimated log K_{S0} values in the range of $10^{-39.5}$ to $10^{-42.4}$. These differences in the derived solubility are also mirrored in the various estimated Gibbs free energy of formation, $\Delta_fG°$, ranging approximately from −9076 to −9100 kJ/mol) and enthalpy of formation, $\Delta_fH°$, from −9792 to −9839 kJ/mol, as shown in Table 1. The differences observed between the solubility products and Gibbs free energies reported by Hirsch and Lothenbach [6] and in this study can be largely attributed to the different methodologies used, even when the same original concentrations from Dickson et al. [28] were considered. These differences are particularly significant as the measured Ca and Si concentrations and pH values show substantial variations, such that the calculated log K_S was strongly influenced by the identification of outliers and whether the measured pH values were considered or not. In our study, the solubility product is calculated individually for each batch and sampling time based on the measured Ca and Si concentrations and pH values, and the mean value is reported, after sorting out obvious outliers. In contrast, Dickson et al. [28] calculated K_S from the mean of all Ca and Si concentrations measured at each temperature although their measured data showed considerable variations, ignoring the measured pH values. Hirsch and Lothenbach [6] recalculated in the solubility product from selected reported Ca and Si concentrations also neglecting the measured pH values and assuming a long-term instability of gyrolite with respect to xonotlite. Blanc et al. [9] derived their stability data reported in Thermochimie and Thermoddem database [30] based on relative stabilities of the phases at high temperatures. These differences in data treatment and calculation procedures explain the observed variations among the datasets. The entropy (S) values reported in literature vary between 590 and 746 J/mol/K, while the heat capacity (C_p) values vary between 536 and 685 J/mol/K (Table 1). All the entropy and heat-capacity values listed in Table 1 are estimated and not experimentally measured values. To the best of our knowledge, no direct measurements of enthalpy or heat capacity data are available in open literature. Thermodynamic data for gyrolite reported by Babushkin [27], Blanc et al. [9], and Hirsch and Lothenbach [6] are presented here in Table 1 after being recalculated from the formula $Ca_2Si_3O_{7.5}(OH)_2\cdot H_2O$ to $Ca_4Si_6O_{15}(OH)_2\cdot 4H_2O$. No information regarding the stability of substituted gyrolite (i.e., with Fe(III)) is available.

The synthesis of gyrolite is complex and involves preparing a suspension of CaO and SiO_2, which is then aged under hydrothermal conditions between 120°C and 200°C and saturated steam pressure (between ∼2 to ∼15 bar) [32]. Temperatures below 150°C result in longer synthesis times, while temperatures above 200°C lead to the initial formation of metastable gyrolite, which recrystallizes to truscottite ($Ca_{14}Si_{24}O_{58}(OH)_8\cdot 2H_2O$) with time [16, 33, 34]. The use of amorphous SiO_2 accelerates the formation of gyrolite, as it facilitates the development of a low Ca/Si ratio in solution [35], while the use of the less soluble quartz lowers the Si concentration in solution favoring the (initial) formation of phases with higher Ca/Si ratios, such as tobermorite ($Ca_5Si_6O_{17}\cdot 5H_2O$) or xonotlite ($Ca_6Si_6O_{17}(OH)_2$) [35–37].

TABLE 1 | Thermodynamic data and solubility products for gyrolite ($Ca_4Si_6O_{15}(OH)_2(H_2O)_4$) at standard conditions (T = 25°C and 1 bar pressure) are reported in the literature.

	$\Delta_f G^\circ$ (kJ/mol)	$\Delta_f H^\circ$ (kJ/mol)	S (J/mol/K)	C_p (J/mol/K)	log K_S[a]	Method[b]
Babushkin et al. [27]	−9084.7	−9839.5	536	590	−41.0[d]	est.[c]
Dickson et al. [28]					−51.1[e](−39.6[f])	meas.
0.1 µm filtered [28]					−47.2[e] (−40.9[f])	meas.
Duplicate [28]					−41.2[e] (−40.0[f])	meas.
VBT[g] [31]			726±54	679±100		est.[g]
Blanc et al. [9]	−9100.1	−9836	619	652	−42.4[i]	est.[h]
Hirsch et al. [6]	−9076	−9792	685	746	−39.5[i]	est.[h]
This study	−9124.5 ± 56[j]	−9840.5 ± 64[k]	685 [j]	746 [j]	−48 ± 1[j]	meas.[j]

[a] Solubility product of gyrolite referring to $K_{S,\ gyrolite} = \{Ca^{2+}\}^4\{HSiO_3^-\}^6\{OH^-\}^2\{H_2O\}$.

[b] Method: est. = estimated and meas. = measured.

[c] $\Delta_f G$ and $\Delta_f H$ were estimated from mean bond energies and C_p as a function of the temperature (C_p = a+bT+cT^{-2}) [27].

[d] log K_S calculated from $\Delta_f G^\circ$.

[e] Natural gyrolite from India; mean solubility product based on the solubility product calculated individually from the total measured concentrations and pH reported in [28] for each sampling time. Some of the values between 28 and 113 days were considered outliers and excluded.

[f] Natural gyrolite form India; solubility product calculated from the mean of all Ca and Si concentrations measured at each temperature converted here from $K_S = \{Ca^{2+}\}^2\{Si(OH)_4{}^0\}^3/\{H^+\}^4/\{H_2O\}^4$ reported in [28], to $K_{S,\ gyrolite} = \{Ca^{2+}\}^4\{HSiO_3^-\}^6\{OH^-\}^2\{H_2O\}$.

[g] VBT: volume-based thermodynamic. Estimated from Glasser and Jenkins [31] where S = 1579*V_m+6 and Cp = 1465*V_m+11. V_m is the molar volume of gyrolite corresponding to 0.456 nm^3/mol [16].

[h] Estimated based on observed phase stability and experimental data from Dickson et al. [28].

[i] Recalculated here from $K_S = \{Ca^{2+}\}^2\{Si(OH)_4{}^0\}^3/\{H^+\}^4/\{H_2O\}^{4.}$

[j] Calculated from undersaturation experiments. Cp and S are taken from Hirsch and Lothenbach [6].

[k] $\Delta_f H$ calculated from: $\Delta_f G + T\cdot\Delta S$.

TABLE 2 | Chemical composition (by XRF) and loss on ignition (LOI) of raw materials.

	Content, wt.%								
Material	**CaO**	**MgO**	**SiO_2**	**Fe_2O_3**	**Al_2O_3**	**P_2O_5**	**TiO_2**	**LOI**	**Other**
$SiO_2\cdot nH_2O$	0.10	—	81.3	—	—	0.18	0.02	18.3	0.10
$CaCO_3$	55.6	0.29	0.05	0.01	0.02	0.03	—	43.7	0.22

In the CaO used for the synthesis of gyrolite, impurities can be present. CaO is generally prepared from the calcination of limestone ($CaCO_3$), which can contain, in addition to calcite, also secondary minerals such as dolomite ($CaMg(CO_3)_2$), quartz, and other silicates such as clay minerals, which add SiO_2, Al_2O_3, Fe_2O_3, and alkalis. The presence of MgO, SiO_2, Al_2O_3, and Fe_2O_3 is expected to affect the synthesis and the stability of gyrolite. While it is well investigated that Al can stabilize tobermorite [38–40] and Mg stabilizes xonotlite [41], little is known about the effect of Fe or Al on gyrolite. Miyak et al. [24] were able to synthesize Al-substituted gyrolite using a zeolite (mordenite) as an Al-source. Baltakys et al. [42] observed that the use of γ-Al_2O_3 retarded the formation of gyrolite, while the combination of γ-Al_2O_3- and Na_2O-stabilized gyrolite [42]. It has been observed that Fe(III) can adsorb on gyrolite [26, 43], without changing its crystal structure, but studies on the effect of Fe(III) on the stability of gyrolite are not available in the open literature.

This study aims to determine the potential uptake of Fe(III) in the structure and its effect on the solubility of both pure and Fe(III) substituted gyrolite, based on determining the solubility from undersaturation experiments. These findings contribute to a deeper understanding of the thermodynamic behavior of pure and Fe(III)-substituted gyrolite, with potential implications for both theoretical and practical applications as an absorbent material.

2 | Materials and Methods

2.1 | Synthesis Procedure

Gyrolite was synthesized hydrothermally, in the absence and presence of Fe(III) in the form of nitrate ($Fe(NO_3)_3$), as detailed in [44]. Iron was added as $Fe(NO_3)_3$ to ensure a high solubility of Fe^{3+}. The dry primary mixture of fine-grained $SiO_2\cdot nH_2O$ (Eurochemicals, Lithuania; Table 2) and calcium oxide (produced by burning $CaCO_3$ [Sigma-Aldrich, Germany; Table 2] at 950°C for 1 h; free CaO: 97.9%) was homogenized for 45 min at 35 rpm in a tubular mixer.

TABLE 3 | Composition of primary mixtures.

Molar ratio CaO/SiO_2	0.68[a]			
CaO (g)	0.68			
$SiO_2{\cdot}nH_2O$ (g)	1.32[b]			
mg Fe^{3+}/g ($CaO+SiO_2$)	0	25	50	75
Total Fe^{3+} in solution, mmol/L	0	45	89	135
Molar ratio Fe/Si	0	0.05	0.10	0.15

[a] molar ratio calculated considering that the silica source contains only 81.3 wt.% SiO_2 (corresponding to 1.07 g of added SiO_2), as reported by the XRF data in Table 2.

[b] corresponding to 1.07 g SiO_2.

Two grams of the mixture were placed in a PTFE vessel, with 20 g of iron(III) nitrate solutions (2.5, 5, 7.5 g/L of Fe^{3+}, corresponding to pH values of 2.42, 2.27, and 2.18, respectively) or deionized water. The iron concentration in the resulting solution was 45, 89, or 135 mmol/L, corresponding to 0, 25, 50, or 75 mg of Fe^{3+} per gram of $CaO+SiO_2$. The detailed composition of primary suspensions is given in Table 3.

The vessel with the suspension was placed in a Parr Instrument autoclave (1-L volume), where the synthesis was carried out at 200°C for 72 h without any stirring of the suspension. The 200°C (steam pressure of ~17 bar) was reached within 2 h. After hydrothermal treatment, the obtained products were filtered (pore size 2–3 µm), rinsed with ~10 mL of acetone, dried at 50°C ± 5°C for 24 h, crushed by hand in an agate mortar, and sieved (<80 µm) before characterization.

Hydroandradite (HA, $Ca_3Fe_2(SiO_4)(OH)_8$) was also synthesized for comparison, adapting the procedure reported in [45]. In 200 g of 1 M KOH solution, 2.12 g of Na_2SiO_3 was first dissolved to ensure complete dissolution. Then, a mixture of 12.32 g of $Ca(NO_3)_2{\cdot}4H_2O$ and 14.05 g of $Fe(NO_3)_3{\cdot}9H_2O$ was added. The suspension was heated in a 200 mL Teflon container at 110°C for 8 days. After cooling down to room temperature, the solid phase was filtered and dried in a freeze-drier (−60°C and 0.0010 mbar) before characterization by XRD, TGA, and FT-IR. The resulting solid was a faint shade of pink, indicating the presence of traces of iron hydroxide phases.

2.2 | Solid Phase Characterization

2.2.1 | x-Ray Diffraction

Powder x-ray diffraction (XRD) measurements were conducted on a PANalytical X'Pert Pro instrument with Bragg-Brentano geometry and equipped with an X'Celerator detector using CoK_α (1.78901Å) radiation. The samples were back-loaded in 27 mm sample holders, and the measurements were recorded from 5° to 90° 2θ with a step size of 0.017° 2θ and a measurement time of 45 min. The radius of the goniometer was 240 mm and the following setting was used: Fe-filter, 15 mm mask, ½°fixed divergent slit, 1°antiscatter slit of and 0.05 rad soller slit on the incident beam side, and 5.5 mm antiscatter slit, 0.05 rad soller slit and the X'Celerator detector on the diffracted beam side. Voltage and current were set at 45 kV and 40 mA, respectively.

The XRD data were evaluated with Rietveld analysis combined with an external standard method [46] using CaF_2 to detect the total amount of amorphous and/or unidentified phases. Rietveld refinement was done using TOPAS V.7 with the following cif-files: ICSD 68199 (gyrolite) [16], ICSD 83715 (hydroandradite) [47], ICSD 40107 ($CaCO_3$) [48], and ICSD 41413 (CaF_2) [49]. The refined parameters included crystal lattice constants, scale factors, and atomic position in the gyrolite interlayer sheet (X) [17], anisotropic crystal growth was also taken into account [50]. The cif-file for xonotlite identification was prepared as described in [41] from the data of the xonotlite polymorph Ma2b2c [51], which is known to be the stable polymorph forming during xonotlite synthesis [52].

Crystallite sizes were estimated from the Lorentzian size-broadening component (CS_L) obtained by Rietveld refinement using TOPAS with the following command: *LVol_FWHM_CS_G_L (k, lvol, kf, lvolf, csg, csl).*

2.2.2 | Thermogravimetry

Around 30 mg of the sample was filled into a 150 µL corundum crucible. The thermogravimetric analysis (TGA) was conducted under N_2 atmosphere (20 mL/min) with a Mettler Toledo TGA2 instrument from 30°C to 980°C at a heating rate 20 K/min.

2.2.3 | Fourier Transform Infrared Spectroscopy

A Bruker Tensor 27 FTIR spectrometer was used to obtain Fourier transform infrared (FT-IR) spectra of the samples. The spectra were collected in transmission mode with a resolution of 4 cm^{-2} and by averaging 32 scans in the range from 340 to 4000 cm^{-1}. OPUS 8.2 SP2 software was used for processing the recorded spectra and performing baseline correction. The intensities of the spectra were normalized to that of the band at ~459 cm^{-1}.

2.2.4 | Scanning Electron Microscopy

An ESEM Quanta 650 instrument was used to perform scanning electron microscopy (SEM). Low vacuum mode (0.80 mbar) to minimize charging effect was used. Secondary electron (SE) images were acquired by using a large field detector (LFD) with an electron beam of 10 kV and a spot size of 3.0 mm. Powdered samples were dispersed with the use of a spatula on the stubs using conductive carbon adhesive tape.

2.3 | Solubility Experiments

2 g of the synthesized gyrolite or Fe-gyrolite sample were dispersed in 200 mL of Milli-Q water to determine the equilibrium concentration in solution from undersaturation at 20°C and 80°C. For each temperature, three replicates were prepared and placed in 250 mL PET vessels for the samples equilibrated at 20°C, which were kept in a climatized chamber at 20°C on a shaking table

moving at 100 rpm. The 80°C samples were prepared in Teflon vessels, stored in an oven at 80°C, and shaken for a few seconds once a day by hand. After 1, 7, 28, 56, and 120 days, 2 mL of the solution was collected with a syringe from each batch and filtered with a 0.2 µm nylon filter. This aliquot was used for ICP-OES analysis, 0.2 µm pore size was used to ensure that no solid particles enter the ICP instrument, avoiding contamination or potential damage.

After 120 days, the solid phase was gained from the remaining suspension by filtration with a 0.45 µm filter in a glove box filled with N_2 to minimize carbonation. The solid was collected, freeze-dried, and then ground with an agate mortar to separate agglomerates. The freeze-drying method was used to rapidly remove the free water from the samples and to minimize carbonation. Finally, the dried solid was characterized using XRD, TGA, and FT-IR spectroscopy.

2.4 | Aqueous Phase Characterization

The filtrated solutions collected from the suspensions were diluted by a factor of 1:10 and 1:20 with a 2% ultra-pure HNO_3 solution. The total concentrations of Si, Ca, and Fe were determined by inductively coupled plasma optical emission spectrometry (ICP-OES MY19451002 Agilent instrument) with a plasma flow of 121 L/min and a nebulizer flow of 0.71 L/min.

pH was measured on an aliquot of the undiluted solution at laboratory temperature (20°C–23°C) with a Knick pH meter (pHMeter 766) equipped with a Knick SE100 electrode. The calibration was done based on a series of standard solutions: pH = 4 (EMD Millipore Corporation buffer solution 1.99001), pH = 7 (EMD Millipore Corporation buffer solution 1.99002), pH = 9 (EMD Millipore Corporation buffer solution 1.99003), and pH = 12 (EMD Millipore Corporation buffer solution 1.99022). To assess whether filtration had an effect on the measured pH values, some pH values were also measured in the unfiltered suspensions; there was no significant difference (<0.1 pH unit) between the pH values measured in the unfiltered suspensions and the filtered solutions.

2.5 | Thermodynamic Modeling

Thermodynamic modeling was conducted using the geochemical software GEMS-Selektor v.3.9. GEMS is a geochemical modeling tool that utilizes Gibbs free energy minimization algorithms to calculate the equilibrium state of a chemical system based on its initial bulk composition [53, 54]. GEMS is equipped with a thermodynamic database for aqueous and solid species: the PSI-Nagra thermodynamic database [55]. This is supplemented with thermodynamic data for cement mineral phases from the Cemdata18 database [56], the CASH+ model [57] used to describe the solubility of poorly ordered C-S-H phases, and thermodynamic data for crystalline calcium silicates from Hirsch and Lothenbach [6].

The measured total concentrations of Si, Ca, and Fe were utilized to calculate the activities of Ca^{2+}, $HSiO_3{}^-$, $FeO_2{}^-$, H_2O^0, and OH^- in solution using GEMS following the procedure established in previous studies [38, 41, 52]. The activity of a given species *i* was determined as $\{i\} = \gamma_i \cdot m_i$, where $\{i\}$ represents the activity of the species *i*, γ_i is the activity coefficient calculated based on the extended Debye–Hückel equation (Equation 1), m_i is the molality (mol/kg H_2O) of the species *i*, z_i is the charge of species *i* and *I* is the effective ionic strength:

$$\log \gamma_i = -\frac{A_y z_i^2 \sqrt{I}}{1 + B_y a_i \sqrt{I}} + b_y I \tag{1}$$

In this equation, A_y and B_y are Debye–Hückel solvent parameters dependent on temperature and pressure, and they are defined in the GEMS software [53]. The values $a_i = 3.72$ Å and $b_y = 0.64$ were used, corresponding to a NaCl electrolyte according to Helgeson et al. [58].

The solubility product of gyrolite is calculated based on the dissolution reaction as follows:

$$\mathrm{Ca_4Si_6O_{15}(OH)_2(H_2O)_4} \leftrightarrow \mathrm{4Ca^{2+} + 6HSiO_3^- + 2OH^- + H_2O} \tag{2}$$

$$\log\left(\mathrm{K_S}\right) = 4 \cdot \log\left(\left\{\mathrm{Ca^{2+}}\right\}\right) + 6 \cdot \log\left(\{\mathrm{HSiO_3^-}\}\right) + 2 \cdot \log(\{\mathrm{OH^-}\}) + \log\left(\{\mathrm{H_2O}\}\right) \tag{3}$$

The solubility product of gyrolite obtained at 20°C and 80°C, together with the trend of the solubility product against the temperature, were used to extrapolate the solubility product of gyrolite at standard conditions (T = 25°C and p = 1 atm) using estimated entropy, *S*, and heat capacity, C_p, values as given in Table 1. The trend of the solubility product against the temperature is obtained from the built-in three-term temperature extrapolation.

$$\log\ K_{S,T} = A_0 + A_2 T^{-1} + A_3 \ln T$$

where A_0, A_2, and A_3 are related to the standard value of entropy, heat capacity, and enthalpy of reaction [59] according to Equations (4)–(6):

$$A_0 = \frac{0.4343}{R} \cdot \left[\Delta_r S^0_{T_0} - \Delta_r C p_{T_0} \left(\ln T_0 + 1\right)\right] \tag{4}$$

$$A_2 = \frac{0.4343}{R} \cdot \left(\Delta_r H^0_{T_0} - \Delta_r C p_{T_0} T_0\right) \tag{5}$$

$$A_3 = \frac{0.4343}{R} \cdot \Delta_r C p_{T_0} \tag{6}$$

Using the solubility product derived for 25°C, the Gibbs free energy of reaction and formation was calculated based on aqueous speciation as reported in PSI-Nagra thermodynamic database [55]. The heat capacity (C_p) and entropy (S) values were taken from Hirsch and Lothenbach [6].

In addition, to assess whether solid phases dissolved or precipitated, saturation indices (SI) with respect to gyrolite, hydroandradite, and amorphous silica, were calculated by GEMS based on Equation 7.

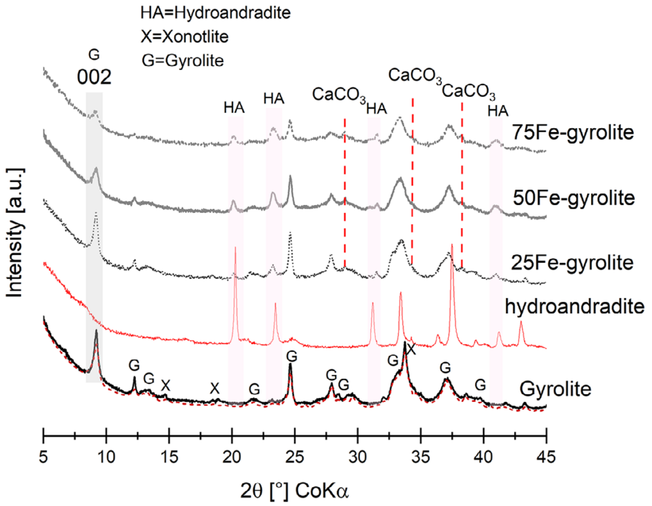

FIGURE 2 | x-Ray diffraction patterns of synthesized pure gyrolite compared to gyrolite with different amounts of iron and the synthesized hydroandradite. The 002 reflection represents the basal spacing of gyrolite. The dotted red line represents the calculated intensity from the Rietveld refinement.

$$SI = \log\left(\frac{IAP}{K_{SO}}\right) \qquad (7)$$

where K_{SO} is the theoretical solubility of gyrolite and hydroandradite as detailed in [6, 45] and *IAP* is the corresponding ion activity product derived from the measured total elemental concentration in the solution.

The expected long-term phase composition was calculated using the thermodynamic database of Hirsch and Lothenbach [6] combined with the gyrolite data derived in this study, the hydroandradite data derived in Dilnesa et al. [45], goethite and hematite from the recent version of the PSI/TDB [60], and xonotlite from [41, 52]. For andradite ($Ca_3Fe_2Si_3O_{12}$), the recently determined thermodynamic data from Geiger and coworkers were used: heat capacity, $C_p° = 347$ $J{\cdot}K^{-1}{\cdot}mol^{-1}$, entropy $S°_m = 325$ $J{\cdot}K^{-1}{\cdot}mol^{-1}$ [61], and enthalpy of $\Delta_f H°_m = -5763.3$ $kJ{\cdot}mol^{-1}$ [62]. An ideal solid solution was assumed between hydroandradite and andradite.

3 | Results and Discussion

3.1 | Pure Gyrolite

The x-ray diffraction patterns (bottom of Figure 2) confirm the formation of gyrolite in the sample without iron, as indicated clearly by the reflection of the basal spacing of gyrolite (002: 2θ CoK$\alpha = 9.3°$ and $d = 11$ Å). In addition to gyrolite, a small amount of xonotlite was observed.

Figure 3 presents a comparison of the FT-IR spectrum of the gyrolite sample without iron with the spectrum of xonotlite. The primary gyrolite signals corresponding to the intertetrahedral bending of O–Si–O linkages are observed between 460 and 790 cm^{-1}. Signals at 1002, 1034, and 1131 cm^{-1} are attributed to the asymmetric stretching of the Si–O bond in Q^3 tetrahedra in gyrolite [63, 64]. In addition, a strong signal at 969 cm^{-1} and a shoulder at ~921 cm^{-1} indicate the presence of some xonotlite [52, 64], which was also observed by XRD analysis (Figure 2) and TGA (Figure 4). Another characteristic signal of gyrolite is the stretching vibrations of the OH groups connected to Ca (Figure 3). This bond produces a narrow signal at 3637 cm^{-1}, while molecular water in the interlayer is visible as a broad band at 3450 cm^{-1}, along with a signal at 1634 cm^{-1} due to the bending vibration of water [65].

The TGA of gyrolite shows water loss at two different temperatures upon heating, as illustrated by the solid lines in Figure 4. Between 80°C and 450°C, approximately 9 wt.% of water is released from the interlayer [14]. Subsequently, between 550°C and 850°C, an additional 3 wt.% of water is lost due to the decomposition of hydroxyl groups [14]. Notably, gyrolite transforms into β-wollastonite between 700°C and 850°C [14, 33]. In the pure gyrolite sample, there are two weight losses at ~800°C. The first weight loss can be related to gyrolite, while the second one, at higher temperature, can be related to the presence of some xonotlite, which releases water at this temperature as it undergoes transformation to β-wollastonite as well [52, 66].

3.2 | Effect of Fe(III)

Figure 2 shows that the gyrolite reflections in XRD become broader and less intense in the presence of Fe(III), indicating the formation of a less well-ordered or nanocrystalline gyrolite. This is in agreement with previous studies, which have shown that the presence of Fe^{3+} during the formation of tobermorite and xonotlite induces defects in their crystal structure [67, 68]. The peak broadening is also confirmed by the decrease in crystallite size when Fe (III) is present. No significant differences can be observed from the lattice parameters of gyrolite with the addition of iron, suggesting that either none or very small amounts of iron are incorporated into the gyrolite structure (Table 4).

In addition, xonotlite disappears while hydroandradite (HA, $3CaO{\cdot}Fe_2O_3{\cdot}nSiO_2{\cdot}(6\text{-}2n){\cdot}H_2O$) and calcite ($CaCO_3$) are formed. The presence of Fe(III) seems to promote calcite formation. Increasing the iron content in the gyrolite samples leads to a continuous reduction in the amount of gyrolite and to the formation of more hydroandradite, calcite and amorphous phase as summarized in Table 5.

The Fe/Si ratio in the formed hydroandradite can be determined based on the well-known correlation between the amount of incorporated Si and the cell volume of hydroandradite [69]. This analysis enabled us to identify that in tendency the Si content in hydroandradite increased with increasing Fe(III) content: $Ca_3Fe_2(SiO_4)_{0.83}(OH)_{8.68}$ (148.7 cm^3/mol) in 25Fe-gyrolite, $Ca_3Fe_2(SiO_4)_{0.67}(OH)_{9.32}$ (150.1 cm^3/mol) in 50Fe-gyrolite, and $Ca_3Fe_2(SiO_4)_{1.03}(OH)_{7.88}$ (147.1 cm^3/mol) in 75Fe-gyrolite (all Si content ± 0.1).

The presence of hydroandradite indicates that Fe(III) is at least partially bound in hydroandradite and not in gyrolite. Mass balance calculations were used to derive the amount of iron available to be incorporated into the gyrolite structure, based on the initial amount of iron added and the quantity of hydroandradite

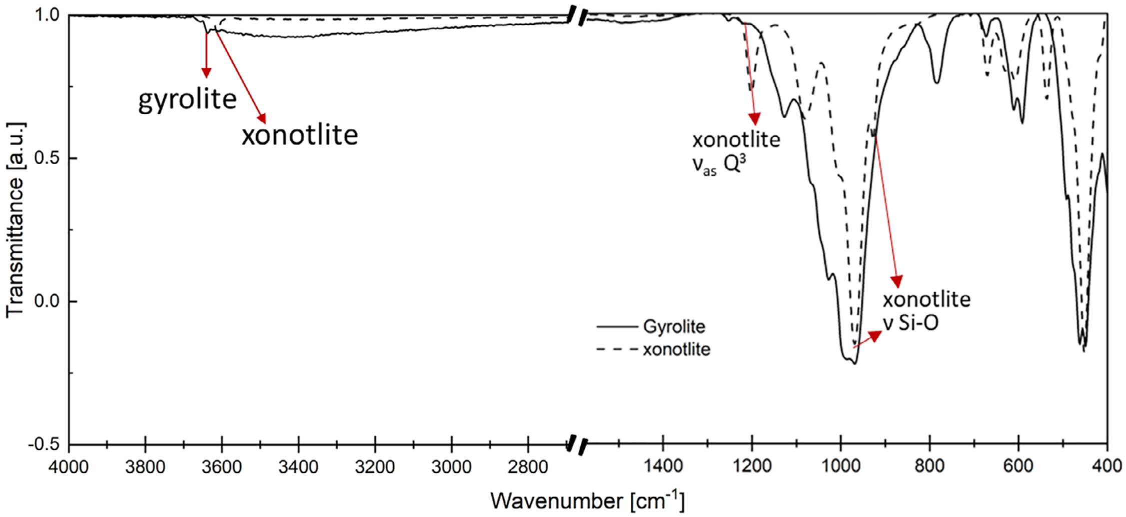

FIGURE 3 | FT-IR spectrum of the gyrolite sample without iron compared to that of pure xonotlite in the range of 4000–400 cm^{-1}.

TABLE 4 | Cell parameters and crystallite sizes of the gyrolite structure obtained from Rietveld refinement of the XRD data for the synthesized samples, compared with the gyrolite cell parameters reported by Merlino [16].

	No Fe	Experimental (XRD)			
	Merlino [16]	**Gyrolite**	**25Fe-gyrolite**	**50Fe-gyrolite**	**75Fe-gyrolite**
a (Å)	9.74	9.689 ± 0.001	9.712 ± 0.001	9.726 ± 0.002	9.721 ± 0.003
b (Å)	9.74	9.727 ± 0.001	9.719 ± 0.001	9.715 ± 0.002	9.713 ± 0.003
c (Å)	22.40	22.474 ± 0.002	22.489 ± 0.004	22.469 ± 0.006	22.438 ± 0.009
α (°)	95.7	95.70	95.21 ± 0.01	95.66 ± 0.02	95.45 ± 0.03
β (°)	91.5	91.50	91.68 ± 0.01	91.44 ± 0.02	91.55 ± 0.03
γ (°)	120	120	120	120	120
Volume (Å^3)	1824.13	1818.1 ± 0.3	1825.4 ± 0.5	1822.9 ± 0.7	1819.5 ± 1.1
Crystallite size (nm)	—	40.7 ± 0.9	33.7 ± 0.6	25.7 ± 0.6	19.9 ± 0.6

formed ($Fe(III)_{res}/Fe(III)_{initial}$ in Table 5). For the 25Fe-gyrolite and 50Fe-gyrolite samples, all Fe(III) seems to be incorporated in hydroandradite. Only for the 75Fe-gyrolite sample, 26 mol% of the initial iron is not bound in hydroandradite and could thus be available to be incorporated into either gyrolite or the amorphous phase. However, no noticeable shifts in the gyrolite XRD reflections or changes in the lattice parameters (Table 4) are observed across all samples, regardless of iron content, which suggests that either no iron or only very small amounts are incorporated into the gyrolite structure or that their incorporation does not affect the structure. No other crystalline Fe-bearing phases such as hematite or goethite were observed. The color of the samples goes from white (sample without iron) to orange/reddish (samples with iron(III)), emphasizing the formation of some Fe-hydroxides (Figure S1), even if they were not observed by XRD, which might be due to their small amount or due to their low crystallinity.

Hydroandradite has a much higher Ca/Si ratio of ≈3 than gyrolite (Ca/Si = 0.67), such that the formation of hydroandradite can be expected to promote the formation of amorphous SiO_2. The presence of unreacted silica may also result from the low pH of 2.2 to 2.4 in the starting $Fe(NO_3)_3$ solution, as silica exhibits limited solubility in acidic environments. Mass balance calculations indicate that in the 50Fe-gyrolite sample, all CaO is present in gyrolite, hydroandradite, and calcite, while not all the initial SiO_2 is bound in those phases, confirming the presence of amorphous silica (Table 5). In the 75Fe-gyrolite sample, where the amorphous content is high, mass balance calculations indicate that not all the initial Ca is bound in gyrolite and hydroandradite, such that the amorphous phase is silica or a silica-rich calcium silicate hydrate with a total Ca/Si = 0.4, probably containing the residual iron (hydr)oxide as well.

Figure 5 shows the effect of Fe(III) on the FT-IR spectra of gyrolite, which confirms that xonotlite is absent in the samples containing iron. The second derivative of the transmittance shows that there are no evident shifts of the gyrolite signals, suggesting that no or very little of Fe(III) enters the gyrolite structure. With increasing amounts of Fe(III), the sharp peak at 3637 cm^{-1} related to OH vibrations in gyrolite becomes broader and less distinct, confirming the formation of a more disordered gyrolite, while the increased intensity of the band at 3450 cm^{-1} suggests

TABLE 5 | Quantification based on Rietveld refinement of the XRD diffraction of the pure gyrolite samples and of those with different amounts of Fe(III) added.

	Gyrolite (wt.%)	Hydroandradite (wt.%)	Calcite (wt.%)	Xonotlite (wt.%)	Amorphous[a] (wt.%)	$Fe(III)_{res}/Fe(III)_{initial}$ (%)	$Si_{res}/Si_{initial}$ (%)
Gyrolite	90.6	—	—	9.4	—	0	0
25Fe-gyrolite	86.8	13.1	0.1	—	—	0	0
50Fe-gyrolite	75.6	22	0.03	—	2.4	0	30
75Fe-gyrolite	45.9	20.2	1.2	—	32.7	26	54

Note: Residual iron (= iron not in hydrogarnet) is reported as mol.% and expressed as molar fraction between the residual iron ($Fe(III)_{res}$) and the total added amount of iron used for the synthesis ($Fe(III)_{initial}$). Furthermore, the distribution of the fraction of silica not present in gyrolite and xonotlite (Si_{res} /$Si_{initial}$) is given. Standard error is 5%.

[a] Mass balance calculation indicates that for 50Fe-Gyrolite, mainly the presence of SiO_2, while the amorphous phase of 75Fe-Gyrolite exhibits a molar Ca/Si of 0.4 and Fe/Si of 0.1.

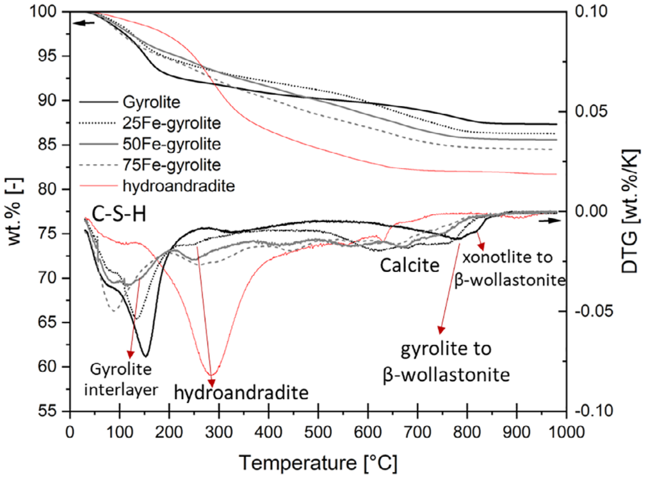

FIGURE 4 | TGA and differential TGA data of pure gyrolite, gyrolite samples with varying Fe content, and hydroandradite (red line).

higher water incorporation, likely due to the presence of the amorphous phase and hydroandradite. In particular, the small narrow band at ~3610 cm^{-1}, close to that of gyrolite at 3637 cm^{-1} (Figure 5b), is characteristic of the OH stretching vibrations in the hydroandradite structure, along with the molecular water stretching band at ~3560 cm^{-1} [70]. With increasing Fe(III) content, the gyrolite Si–O vibration at 1127 cm^{-1} becomes broader and less evident until it merges with the band at 1032 cm^{-1} signal as a shoulder. The broadening of this signal, along with the signal associated with calcite formation, indicates lower crystallinity of gyrolite formed in the presence of Fe(III). The broadening of the shoulders at ~1090 and ~800 cm^{-1} suggests the presence of amorphous silica [71], in agreement with the observation of an amorphous phase by XRD (Figure 2), as well as with the presence of hydroandradite since it also exhibits a signal between 800 and 900 cm^{-1} (Figure 5a).

The TGA data in Figure 4 shows less interlayer water associated with gyrolite at approximately 150°C if Fe(III) has been added. In the presence of more Fe(III), this signal, as well as the weight loss at ~800°C associated with the transformation into wollastonite, shifts toward lower temperatures. These findings agree with the decreased ordering in gyrolite observed by XRD and FTIR, resulting in thermal decomposition of gyrolite at lower temperatures. The presence of Fe(III) also seems to promote calcite formation, as indicated by the weight loss observed between 600°C and 700°C, consistent with XRD and FT-IR results. The weight loss at ~250°C in the iron-containing samples can be related to the presence of hydroandradite [45].

In summary, XRD, TGA, and FT-IR analyses indicate that the addition of Fe(III) results in less and less-ordered gyrolite, and in the formation of hydroandradite, calcite, and amorphous phases.

SEM images support the XRD, TGA, and FT-IR findings. In Figure S2a, the characteristic plate-like morphology of gyrolite [72] is clearly visible in the absence of Fe(III). With the addition of 2.5 g/L of $Fe(NO_3)_3$ (25Fe-gyrolite) (Figure S2b) Journal, the morphology of gyrolite remains largely unchanged, consistent with the XRD results (Figure 2), which still show well-crystallized gyrolite. Alongside the gyrolite plates, there is some unreacted silica, which shows up as spherical particles [73, 74]. In the gyrolite samples synthesized with 5 (50Fe-gyrolite) and 7.5 g/L (75Fe-gyrolite) of $Fe(NO_3)_3$ (Figure S2c,d), the plate-like structure of gyrolite becomes more difficult to identify, suggesting the presence of less crystalline gyrolite. Furthermore, a higher number of roundish particles is visible, indicating an increased presence of unreacted silica as well as hydroandradite visible as cubic or not well-rounded small particles [75–77], in line with XRD quantification (Table 5).

3.3 | Solubility Experiments

3.3.1 | Structural Changes

To determine the solubility of gyrolite, the synthesized samples were re-equilibrated in water at 20°C and 80°C. After 120 days of undersaturation experiments, the solids were collected via filtration and analyzed to assess whether any new phases might have formed. The XRD patterns of the samples before and after solubility experiments are reported in Figure S3. All samples exhibit the characteristic reflections of gyrolite, highlighted by the presence of the basal spacing reflection at 2θ = Co$K\alpha$ 9.3° (002 reflection, d = 11 Å).

The XRD pattern of pure gyrolite (Figure S3a) shows no significant changes in the amount or structure (Tables 6 and S1)

TABLE 6 | Quantification based on Rietveld refinement of the XRD diffraction pattern of the pure gyrolite samples (three replicates) and those with different amounts of Fe(III) after 120 days of solubility experiment.

Sample	Temperature	Series	Gyrolite wt.%	Hydroandradite wt.%	Calcite wt.%	Xonotlite wt.%	Amorphous wt.%
Gyrolite	20°C	a	91.2	—	0.3	8.5	—
		b	89.8	—	0.2	10.0	—
		c	92.9	—	0.2	6.9	—
	80°C	a	89.6	—	0.4	9.9	—
		b	89.7	—	0.3	10.0	—
		c	91.0	—	0.4	8.6	—
25Fe-gyrolite	20°C	a	90.1	9.4	0.4	—	—
		b	88.9	10.7	0.4	—	—
		c	86.3	13.2	0.4	—	—
	80°C	a	87.5	12.3	0.3	—	—
		b	89.6	10.0	0.4	—	—
		c	85.6	14.1	0.2	—	—
50Fe-gyrolite	20°C	a	77.2	22.7	0.03	—	[x]-
		b	77.2	22.6	0.08	—	[x]-
		c	77.1	22.8	0.05	—	[x]-
	80°C	a	78.2	21.6	0.12	—	[x]-
		b	76.9	23.0	0.05	—	[x]-
		c	78.2	21.7	0.12	—	[x]-
75Fe-gyrolite	20°C	a	69.0	20.6	0.6	—	9.8
		b	59.6	22.0	0.1	—	18.3
		c	65.4	21.3	0.2	—	13.2
	80°C	a	54.9	20.7	0.3	—	24.2
		b	69.7	21.0	—	—	9.2
		c	64.0	22.5	0.1	—	13.3

Note: Standard error is 5%.

[x] 2.4 % of the amorphous phase was observed in the sample before exposure.

of gyrolite and xonotlite during exposure to water, except for the formation of some calcite after 120 days at both 20°C and 80°C (Table 6), indicating some limited carbonation during the experiments or sample handling and drying. Thermogravimetric (TGA) analyses in Figure 6a confirm that gyrolite and xonotlite remain largely unchanged during the solubility experiments, except for the formation of calcite, as indicated by a weight loss at 700°C due to CO_2 release. Also, the sharp FT-IR signal at 3637 cm^{-1}, attributed to the OH^- groups linked to Ca in the gyrolite structure, remains unchanged in the pure gyrolite samples (Figure S4a).

In the iron-containing samples (Figure S3b–d), a rearrangement of gyrolite occurs, as visible in a slight increase of the crystallite size (Figure 7 and Table S1), suggesting recrystallization, particularly for the gyrolite without iron, 25Fe- and 50Fe-gyrolite samples. In agreement with our observations, Hou et al. [78] suggested, based on molecular modeling, that Fe(III) weakens the Si-O bonds and strengthens the Ca-O bonds in the interlayer, introducing defects and reducing the polymerization of silicate chain [68, 79]. Fe(III) has been observed to be incorporated in a poorly crystalline C-S-H structure in an octahedral coordination [80, 81]. Haastrup et al. [67] reported that even a small amount of Fe(III) negatively influences xonotlite crystal growth and formation, leading to defects in the Q^3 sites of the xonotlite structure (typical defect site of xonotlite [82]), and increasing the formation of tobermorite and amorphous phases. It seems probable that the presence of Fe(III) also increases the number of defects in gyrolite, leading to structural changes, as evidenced by the decrease in crystallite size between the gyrolite samples without iron and those containing iron, indicating lower crystallinity in the iron-bearing gyrolite.

In the 0Fe-, 25Fe-, and 50Fe-gyrolite samples, the amount of gyrolite does not change significantly over time during the undersaturation experiments (see Tables 5 and 6). However, in the 75Fe-gyrolite sample, the amorphous phase slightly decreases while the amount of gyrolite increases during re-equilibration, both at 20°C and 80°C. The quantity of hydroandradite remains constant during the solubility experiment in all samples. The

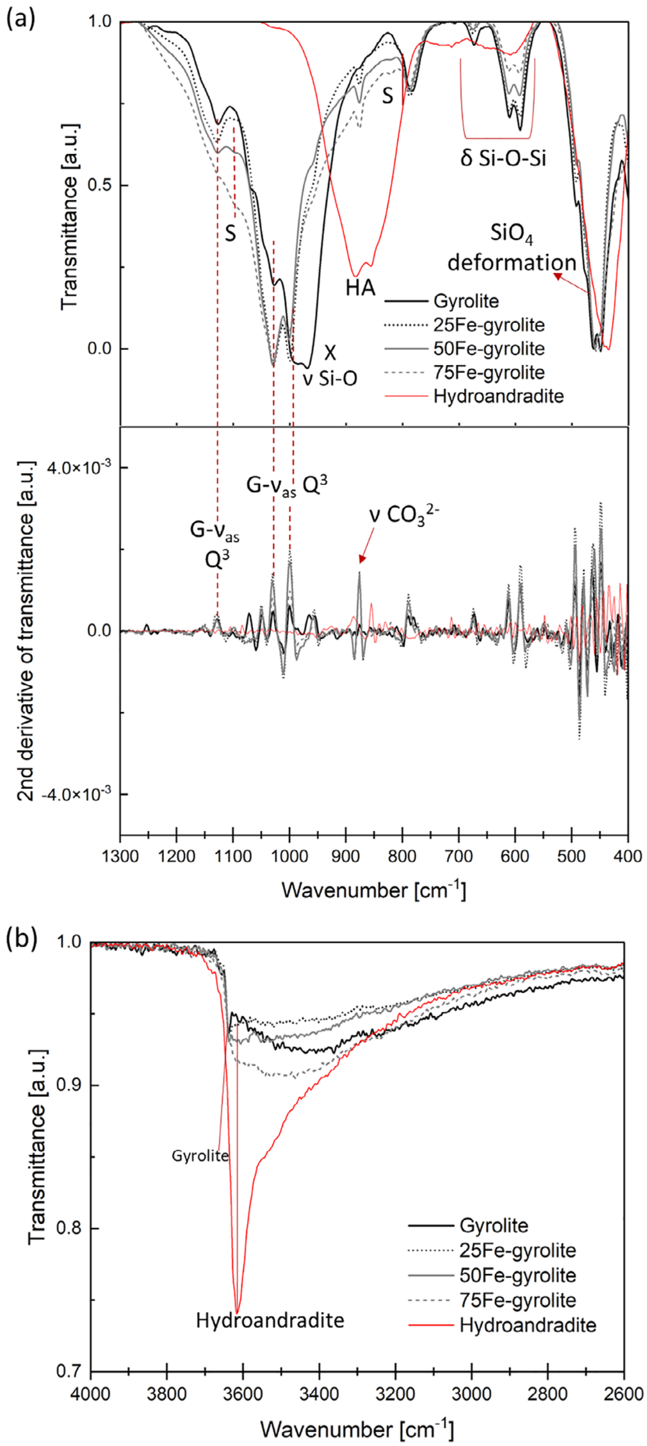

FIGURE 5 | (a) FT-IR spectra and second derivative of transmittance of pure and Fe-containing gyrolite compared with hydroandradite in the range of 1400–400 cm^{-1}; (b) FT-IR spectra of pure gyrolite and Fe-containing gyrolite compared with hydroandradite in the range of 4000–2800 cm^{-1}. G, gyrolite; HA, hydroandradite; S, amorphous silica; X, xonotlite.

amorphous phase decreases as well in the 50Fe-gyrolite sample, probably due to dissolution of the amorphous silica into the solution, which is verified by mass balance calculations considering the amount of Si in solution as well. Also in this case, no evident changes were observed in the lattice parameters of gyrolite during solubility experiments (Table S1).

In agreement with XRD, the TGA data of the Fe-containing samples (Figure 6b–d) show that the weight loss associated with amorphous or less crystalline phases at around 100°C is reduced during the re-equilibration, as well as the weight loss at 400°C–600°C. In contrast, the characteristic weight loss associated with the interlayer water of gyrolite at 150°C becomes more dominant, in particular in the 50Fe- and 75Fe-gyrolite samples (Figure 6c,d). The weight loss at 250°C, related to the presence of hydroandradite, remains unchanged throughout the solubility experiments (Table S2), confirming that hydroandradite is stable, consistent with the XRD findings The FT-IR signals agree with those observations by XRD and TGA, as the band at 3637 cm^{-1}, attributed to OH in gyrolite, increases during the solubility experiments in intensity (Figure S4b–d), indicating either the crystallization of gyrolite and/or the formation of additional gyrolite.

3.3.2 | Aqueous Solution and Gyrolite Solubility

The measured Ca and Si concentrations from the solubility experiments of pure gyrolite conducted in this study are summarized in Table S3. A higher release of Si compared to Ca can be observed, due to the low molar ratio Ca/Si = 0.67 of gyrolite. At 80°C, the Si concentrations are higher, while the calcium concentrations remain similar, tentatively indicating a slightly higher solubility at 80°C. However, at both temperatures, the molar ratio Ca/Si in solution is much lower than that of gyrolite (Ca/Si = 0.2–0.4 in solution vs. Ca/Si = 0.67 of gyrolite), suggesting either binding of some calcium in calcium carbonate, a preferential release of Si, or Ca uptake in the gyrolite structure itself. According to Merlino [16], gyrolite consists of negatively charged layers $[Ca_{12}(Si_8O_{20})_3(OH)_8]^{4-}$ charge-compensated by a positively charged hydrated interlayer $[Ca_2(H_2O)_8\cdot(6+x)H_2O]^{4+}$. Wang et al. [83] measured zeta potential and demonstrated that gyrolite carries a weak negative surface charge if dissolved in water, consistent with the observed cation exchange properties of gyrolite [10]. Cation uptake on the negatively charged silicate surface could explain why there is much less Ca than Si in solution. The measured total Ca and Si concentration increased slowly up to 56 days and stabilized thereafter.

The solubility product of gyrolite was calculated at both 20°C and 80°C using the solubility product obtained from each solution after 56 and 120 days of undersaturation experiments. The calculated ion activity product of gyrolite is $10^{-44.2\pm1.0}$ at 20°C and significantly higher than that at 80°C: $10^{-49.4\pm0.5}$. This difference could be due to the presence of xonotlite in those samples, which also dissolves with time, resulting in a very slow approach to equilibrium, particularly at 20°C, such that equilibrium was not yet reached after 120 days. In fact, the saturation indices (SI) of the solution calculated with respect to xonotlite indicate that the solutions are clearly undersaturated, indicating a potential for xonotlite dissolution, in agreement with the observed slight decrease of the xonotlite content during the re-equilibration (see Table 6).

As reported in Table 1, only one set of solubility measurements of gyrolite was reported in the open literature. Dickson et al.

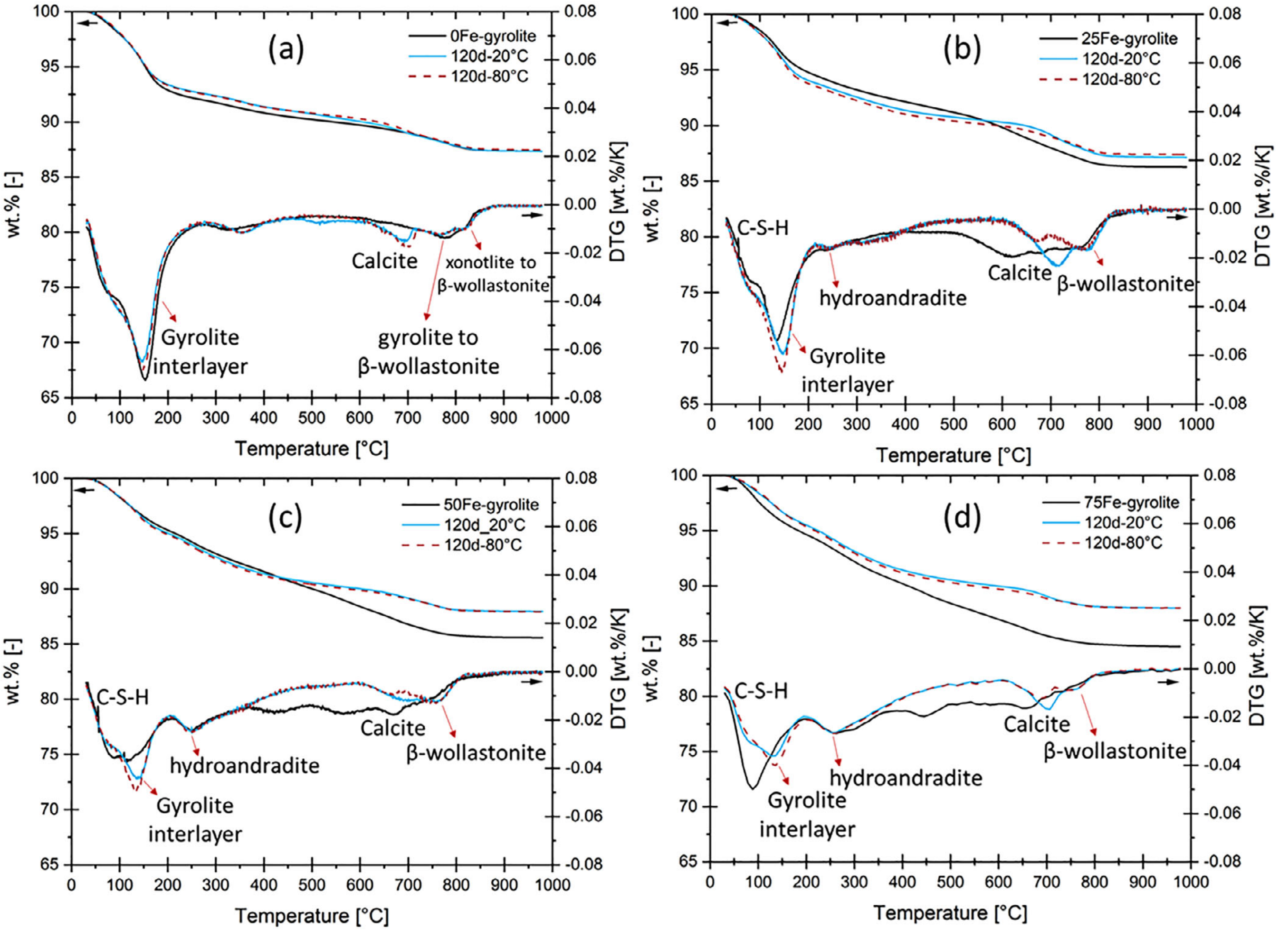

FIGURE 6 | TGA and differential TGA data of: (a) pure gyrolite, (b) gyrolite containing 25 mg of Fe per g of CaO+SiO_2, (c) gyrolite containing 50 mg of Fe per g of Ca+SiO_2, and (d) gyrolite containing 75 mg of Fe per g of CaO+SiO_2.

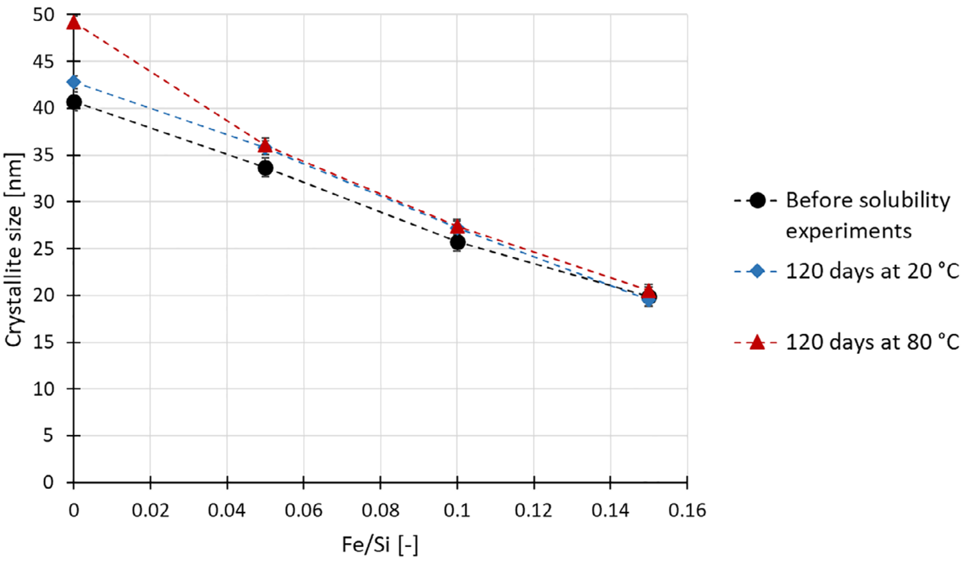

FIGURE 7 | Crystallite size for pure gyrolite and the iron-containing samples plotted as a function of the molar Fe/Si ratio before solubility experiments (black circles) and after 120 days of undersaturation experiments at 20°C (blue rhombuses) and 80°C (red triangles). Error bars are the same size as the data points.

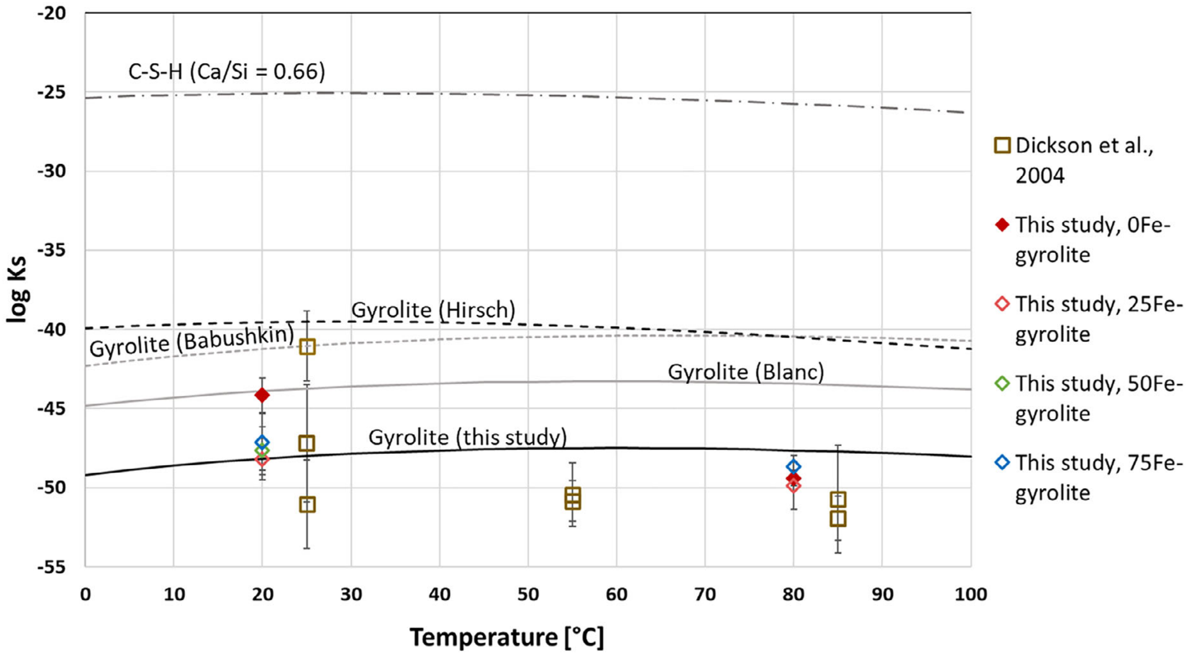

FIGURE 8 | Calculated solubility product of gyrolite, $Ca_4Si_6O_{15}(OH)_2{\cdot}4H_2O$, from the total measured concentration of Ca and Si obtained from this study without iron (red rhombus) and with iron (empty rhombus), and from Dickson et al. [28] (empty squares). The solubility product obtained from estimated thermodynamic data is also reported from: Hirsch and Lothenbach [6], black dashed; Blanc et al. [9], light gray; Babushkin et al. [27], dashed light grey; and this study, black line. The solubility product of C–S–H with Ca/Si = 0.6, calculated using the data of Kulik [84], is given for comparison.

[28] performed this measurement on a natural gyrolite without specifying its chemical composition or impurities present and reported three replicates at 20°C, and two replicates at 50°C and 80°C, which resulted in highly different solubility products (Table 1). These measurements were later used by Hirsch and Lothenbach [6] to estimate the thermodynamic properties of gyrolite. The mean values of the solubility product obtained in our study for gyrolite are displayed in Figure 8 together with the solubility product calculated from Dickson et al. [28]. Two series of Dickson et al. [28] are in good agreement to each other, and they suggest a more stable gyrolite compared to what was reported by Hirsch and Lothenbach [6] and Babushkin et al. [27]. Blanc et al. [9] estimated a more stable gyrolite than Babushkin et al. [27] and Hisch and Lothenbach [6], but less stable than the data derived here.

The measured Ca and Si concentrations of the iron-containing samples show a similar behavior but were affected by the lower pH values. The addition of $Fe(NO_3)_3$ leads to a decrease in pH from 9 to 8 in the samples at 20°C, and from 8 to 6 at 80°C for the highest Fe concentrations (Table S3). This pH reduction could have promoted greater dissolution of calcite, as indicated by TGA and XRD analyses showing reduced calcite content, which might explain the higher amount of total Ca concentration released in solutions in the samples with greater iron content (Table S3). As for the gyrolite samples without iron, the Si concentrations are higher at 80°C than at 20°C. Saturation indices suggest saturation with respect to amorphous silica, consistent with the XRD and FTIR observations that reveal a silicon-rich amorphous phase. In contrast, the saturation indices of hydroandradite indicate undersaturation with respect to hydroandradite, suggesting that the system has not yet reached equilibrium. This aligns well with XRD, FTIR, and TGA data, which indicate a recrystallization of gyrolite during solubility experiments, meaning of a system which probably has not yet reached the equilibrium.

The mean values of the solubility products calculated for gyrolite samples with iron are displayed in Figure 8, with the solubility product of gyrolite without iron. The solubility products of gyrolite with iron are comparable to the solubility of gyrolite without iron at 80°C, but somewhat lower at 20°C, confirming the assumption that the presence of xonotlite led not-equilibrium system at 20°C. The solubility product at 20°C is rather similar to the one at 80°C and to some of the values derived from Dickson et al. [29].

As discussed in Section 2.5, the solubility product as a function of temperature was used to estimate a new thermodynamic dataset for gyrolite. Based on this dataset of gyrolite, the equilibrium binary phase diagram of thermodynamically stable crystalline calcium silicate hydrate phases previously reported by Hirsch and Lothenbach [6] was updated. Using GEMS, the stable phases were identified across a temperature range of 100°C to 250°C for different Ca/Si ratios. By combining the phase assemblages obtained for each Ca/Si ratio over the temperature range 100°C–250°C, the equilibrium phase diagram was constructed (Figure 9). The calculations confirm that at $CaO/SiO_2 \leq 0.67$, gyrolite is thermodynamically stable above 100°C together with quartz due to the excess of Si in this composition range. In the range of CaO/SiO_2 between 0.67 and 1.0, gyrolite and xonotlite are calculated to coexist, which could explain the presence of small amounts of xonotlite in the iron-free gyrolite sample tested in this study. This observation is in agreement with the xonotlite synthesis results reported by Smalakys and Siacucinas [85], who observed that after 3 days of reaction between CaO and amorphous silica at 200°C, both xonotlite and gyrolite were

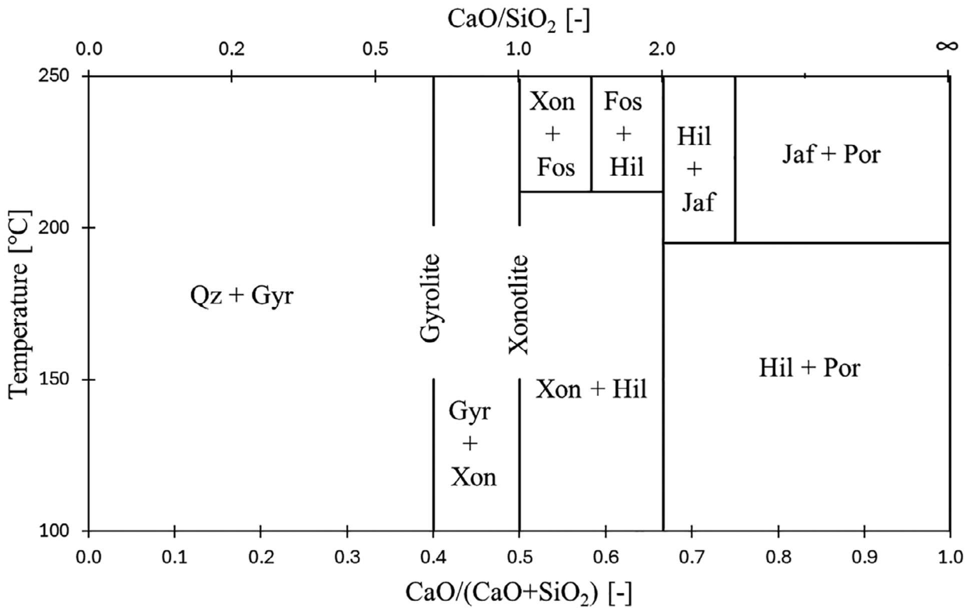

FIGURE 9 | Equilibrium binary phase diagram for the system CaO–SiO_2–H_2O at temperature above 100°C and saturated steam pressure obtained from the thermodynamic datasets for gyrolite from this study (Table 1), xonotlite from [52], and for the phases at higher Ca/Si ratio from Hirsch and Lothenbach [6]. Phase abbreviations are taken from Warr [86] where: Gyr = gyrolite, Qz = Quartz, Xon = Xonotlite, Hil = Hillebrandite, Fos = Foshagite, Jaf = Jaffeite, Por = Portlandite. CaO/(CaO+SiO_2) and CaO/SiO_2 refers to molar ratio.

observed. Similarly, Garbev [64] reported the formation of gyrolite at Ca/Si $\leq$ 0.6 under long-term experiments and temperatures above 100°C, suggesting that gyrolite is a thermodynamically stable phase under these conditions. At Ca/Si = 0.83, Garbev [64] observed the coexistence of xonotlite and gyrolite in long-term experiments, which is consistent with our estimation. Previously, in the range of Ca/Si $\leq$ 1, only xonotlite and quartz were expected to form [6]. At CaO/SiO_2 > 1.0, the updated phase diagram is identical to that presented by Hirsch and Lothenbach [6].

3.4 | Role of Fe(III)

The XRD analyses in this study (Table 5) show that Fe(III) not only lowers the crystallinity of gyrolite but also leads to the formation of hydroandradite, which is related to the high stability of hydroandradite [45]. Hydroandradite is a well-known desilication product, and together with other hydrogrossular phases, it is known to form and stabilize under hydrothermal treatment in the presence of Si, thereby reducing the amount of SiO_2 and CaO in the system available to form other phases [87–89]. The presence of amorphous silica and silica-rich calcium silicate hydrates in the iron-containing samples and the absence of other Fe-bearing hydrates such as hematite or goethite, suggest that Fe(III) preferably forms hydroandradite, reducing the availability of CaO and SiO_2 for the formation of gyrolite. The formation of hydroandradite in iron-containing samples could also have been promoted by the low pH of the initial solution used for the synthesis, which may have delayed the dissolution of SiO_2, as indicated by the presence of a significant amount of unreacted silica in the solid phases. The limited availability of dissolved silica likely favored the initial formation of hydroandradite over gyrolite.

Thermodynamic modeling can be used to simulate which phases are expected to form in the long-term if 0.68 g of CaO and 1.07 g of SiO_2 (Ca/Si = 0.68) are reacted in the presence of 20 g of water at 200°C, as illustrated in Figure 10. A small amount of MgO (0.006 g) was considered, as MgO is present in the $CaCO_3$ used for the synthesis of gyrolite (Table 2) and is known to stabilize xonotlite [41]. The thermodynamic dataset employed for gyrolite corresponds to Fe-free gyrolite, consistent with our experimental observations showing no or very little incorporation of Fe in the gyrolite structure. In the absence of $Fe(NO_3)_3$, only gyrolite and xonotlite are predicted, as illustrated in Figure 10. As the amount of $Fe(NO_3)_3$ increases, the amount of gyrolite decreases, while hydroandradite and amorphous silica begin to form. This trend aligns well with our experimental system, where the samples containing Fe(III) show progressively less gyrolite as well as less crystalline gyrolite together with increasing amounts of hydroandradite and amorphous silica (Table 5). The main discrepancy between the thermodynamic model and the experiments is the amount of xonotlite. GEMS predicts the equilibrium state of the system and therefore reports xonotlite as the most thermodynamically stable crystalline calcium silicate hydrate under the investigated conditions. In contrast, the Fe-bearing synthesized samples do not show any xonotlite formation, indicating that in the experiments, thermodynamic equilibrium was not yet reached.

4 | Conclusion

In this study, the stability range of pure gyrolite ($Ca_4Si_6O_{15}(OH)_2 \cdot 4H_2O$), synthesized without Fe(III) and with three different Fe(III) additions, was investigated. XRD, TGA, and FT-IR analyses revealed that the pure gyrolite contains a small amount of xonotlite, likely due to the known thermodynamic

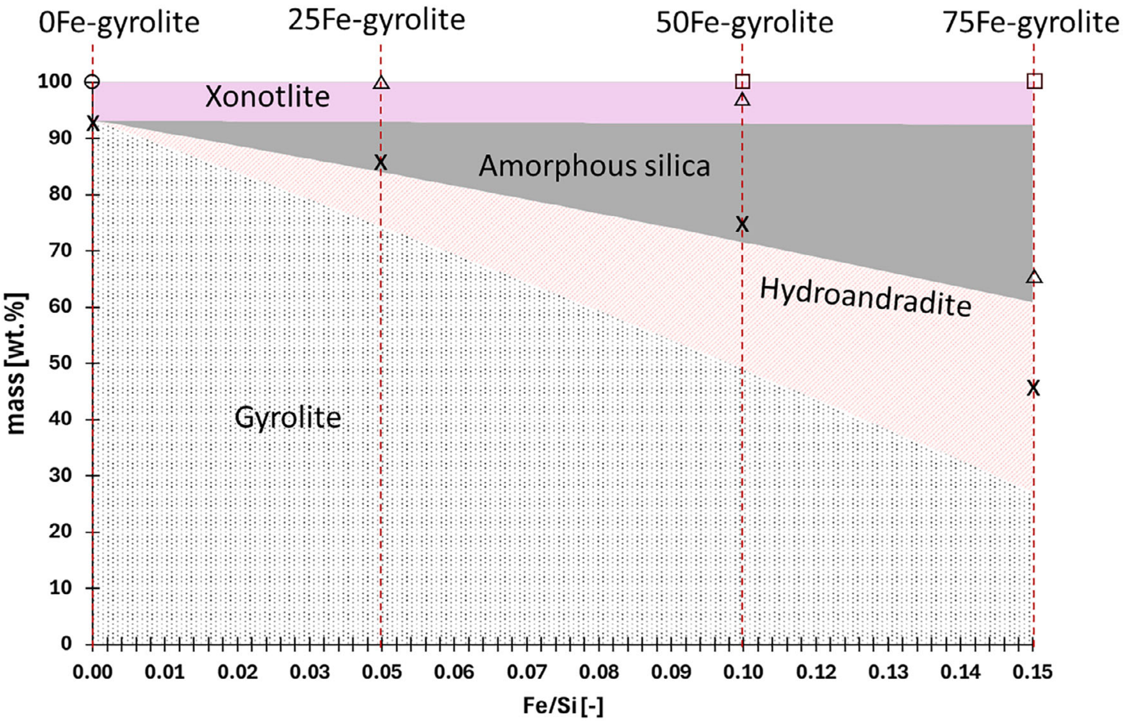

FIGURE 10 | Calculated phase composition of a system where 20 g of water is mixed with 0.68 g of CaO and 1.07 g of SiO_2 (molar Ca/Si = 0.68) at 200°C, with increasing amount of iron nitrate ($Fe(NO_3)_3$ as a function of the Fe/Si molar ratio. Experimental data are plotted for comparison: crosses = gyrolite, circles = xonotlite, triangles = hydroandradite, and squares = amorphous silica.

stability of xonotlite in the long-term experiments and its stabilization in the presence of a small amount of MgO. The addition of Fe(III) lowered the amount of gyrolite as well as its crystallinity, while hydroandradite, calcite, and silica-rich amorphous phases were detected. No iron or only very little was found to be incorporated into the gyrolite structure. Instead, Fe(III) predominantly contributed to the formation of hydroandradite. In the sample with the highest Fe content, ~26 mol.% of Fe did not participate in the formation of hydroandradite and might be present in the silica-rich amorphous phase.

The addition of $Fe(NO_3)_3$ lowered the pH significantly in the Fe-containing samples, which might have affected the uptake of Fe(III) into gyrolite. Further synthesis of gyrolite under increased pH conditions could help to isolate the effect of increased silicon and iron concentrations on phase formation and maybe promote the incorporation of iron into the gyrolite structure.

Undersaturation experiments carried out at 20°C and 80°C indicated that equilibrium between the solid and the aqueous phases was reached after 56 days of undersaturation experiments, both for pure and Fe-containing gyrolite samples. The solubility product determined in this work for pure gyrolite, $10^{-48 \pm 1.0}$, is in good agreement with some of the results of Dickson et al. [28], but is significantly more stable than assumed in several other studies by Hirsch and Lothenbach [6], Blanc et al. [9], and Babushkin et al. [27]. This higher stability of gyrolite suggests that gyrolite could be one of the long-term stable crystalline calcium silicate hydrates, along with xonotlite at a molar Ca/Si ratio below 1.0, as also verified by thermodynamic modeling.

Acknowledgments

The authors thank Fabio Furcas (Empa) and Vincent Hallet (Empa) for helpful discussion, support with XRD interpretation and quantification, and with SEM imaging. The authors also thank Jean-Philippe Boisvert (ETEX), Pavel Lopez (ETEX), and Joyce Mareels (ETEX) for helpful discussion.

Open access publishing facilitated by ETH-Bereich Forschungsanstalten, as part of the Wiley - ETH-Bereich Forschungsanstalten agreement via the Consortium Of Swiss Academic Libraries.

Funding

This study was supported by the ETEX Group.

Data Availability Statement

The data that support the findings of this study are available from the corresponding author upon reasonable request.

References

1. Z. Zhang, X. Wang, and J. Zhao, "Phosphate Recovery From Wastewater Using Calcium Silicate Hydrate (CSH): Sonochemical Synthesis and Properties," *Environmental Science: Water Research & Technology* 5 (2019): 131–139.

2. W. Guan and X. Zhao, "Fluoride Recovery Using Porous Calcium Silicate Hydrates via Spontaneous Ca^{2+} and OH− Release," *Separation and Purification Technology* 165 (2016): 71–77, https://doi.org/10.1016/j.seppur.2016.03.050.

3. J. Wei, T. Zhou, H. Xu, Y. Wang, and B. Wang, "Comparative Study of Silica-Based Porous Materials in the Purification of Radioactive

Wastewater," *Separation and Purification Technology* 357 (2025): 130234, https://doi.org/10.1016/j.seppur.2024.130234.

4. N. J. Coleman, "Interactions of Cd (II) With Waste-Derived 11 Å Tobermorites," *Separation and Purification Technology* 48 (2006): 62–70, https://doi.org/10.1016/j.seppur.2005.07.021.

5. N. J. Coleman, D. S. Brassington, A. Raza, and A. P. Mendham, "Sorption of Co^{2+} and Sr^{2+} by Waste-Derived 11 Å Tobermorite," *Waste Management* 26 (2006): 260–267, https://doi.org/10.1016/j.wasman.2005.01.019.

6. T. Hirsch and B. Lothenbach, "Phase Stabilities and Thermodynamic Properties of Crystalline CaO-SiO_2-H_2O Phases Above 100°C," *Cement and Concrete Research* 177 (2024): 107412, https://doi.org/10.1016/j.cemconres.2023.107412.

7. S. Y. Hong and F. P. Glasser, "Phase Relations in the $CaO–SiO_2–H_2O$ System to 200 C at Saturated Steam Pressure," *Cement and Concrete Research* 34 (2004): 1529–1534, https://doi.org/10.1016/j.cemconres.2003.08.009.

8. H. F. W. Taylor, "Cement Chemistry," (Thomas Telford, 1997).

9. P. Blanc, X. Bourbon, A. Lassin, and E. C. Gaucher, "Chemical Model for Cement-Based Materials: Temperature Dependence of Thermodynamic Functions for Nanocrystalline and Crystalline C–S–H Phases," *Cement and Concrete Research* 40 (2010): 851–866, https://doi.org/10.1016/j.cemconres.2009.12.004.

10. K. Baltakys and T. Dambrauskas, *Application of Synthetic Gyrolite for Adsorption. In Synthetic Gyrolite: A Dual Solution for Wastewater Treatment and Portland Cement* (Springer Nature Switzerland, 2024), 139–209.

11. T. Anderson, "Gyrolite," *Philosophical Magazine Section IV* 1 (1851): 111–115.

12. J. Currie, "Note on Some New Localities for Gyrolite and Tobermorite," *Mineralogical Magazine and Journal of the Mineralogical Society* 14 (1905): 93–95, https://doi.org/10.1180/minmag.1905.014.64.06.

13. F. Fleischmann, "On the Occurrence of Gyrolite in County Antrim," *Mineralogical Magazine and Journal of the Mineralogical Society* 15 (1910): 288–293, https://doi.org/10.1180/minmag.1910.015.71.04.

14. A. Mackay and H. Taylor, "Gyrolite," *Mineralogical Magazine and Journal of the Mineralogical Society* 30 (1953): 80–92.

15. K. Garbev, L. Black, G. Beuchle, and P. Stemmermann, "Inorganic Polymers in Cement Based Materials," *Wasser-und Geotechnologie* 1 (2002): 19–30.

16. S. Merlino, "Gyrolite: Its Crystal Structure and Crystal Chemistry," *Mineralogical Magazine* 52 (1988): 377–387, https://doi.org/10.1180/minmag.1988.052.366.09.

17. A. Baltušnikas, R. Šiaučiūnas, I. Lukošiūtė, K. Baltakys, A. Eisinas, and R. Kriūkienė, "Crystal Structure Refinement of Synthetic Pure Gyrolite," *Materials science* 21 (2015): 111–116, https://doi.org/10.5755/j01.ms.21.1.5460.

18. A. Baltusnikas, I. Lukosiute, R. Levinskas, A. Grybenas, K. Baltakys, and A. Eisinas, "Analysis of Rietveld Method Application for Gyrolite Crystal Structure Refinement," *Materials Science* 18 (2012): 379–384, https://doi.org/10.5755/j01.ms.18.4.3101.

19. K. Momma and F. Izumi, "VESTA 3 for Three-Dimensional Visualization of Crystal, Volumetric and Morphology Data," *Applied Crystallography* 44 (2011): 1272–1276, https://doi.org/10.1107/S0021889811038970.

20. V. Kasperaviciute, K. Baltakys, and R. Siauciunas, "The Sorption Properties of Gyrolite for Copper Ions," *Ceramics-Silikaty* 52 (2008): 95–101.

21. S. El-Korashy, "Cation Exchange of Alkali Metal Hydroxides With Some Hydrothermally Synthesized Calcium Silicate Compounds," *Journal of Ion Exchange* 15 (2004): 2–9, https://doi.org/10.5182/jaie.15.2.

22. K. Baltakys, A. Iljina, and A. Eisinas, "Gyrolite Adsorption of Zn^{2+} Ions in Acidic and Alkaline Solutions," *Materials Science* 21 (2015): 123–128, https://doi.org/10.5755/j01.ms.21.1.5703.

23. K. Baltakys, A. Eisinas, I. Barauskas, E. Prichockiene, and E. Zaleckas, "Removal of Zn (II), Cu (II) and Cd (II) From Aqueous Solution Using Gyrolite," *Journal of Scientific and Industrial Research* 71 (2012): 566–572.

24. M. Miyake, M. Iwaya, T. Suzuki, H. Kakehi, and T. Mitsuda, "Aluminum-Substituted Gyrolite as Cation Exchanger," *Journal of the American Ceramic Society* 73 (1990): 3524–3527, https://doi.org/10.1111/j.1151-2916.1990.tb06491.x.

25. W. Tang, Y. Dai, R. Zeng, et al., "Preparation of Al-Doped Xonotlite and Its Adsorption Properties for Pb (II) in Wastewater," *Desalination and Water Treatment* 190 (2020): 135–146, https://doi.org/10.5004/dwt.2020.25610.

26. S. Zadaviciute, K. Baltakys, and A. Eisinas, "Adsorption Kinetic Parameters of Fe_3 and Ni_2 Ions by Gyrolite," *Materials Science* 21 (2015): 117–122.

27. V. I. Babushkin, G. M. Matveev, and O. P. Mchedlov-Petrosian, *Thermodynamics of Silicates* (Springer-Verlag, 1985), https://doi.org/10.1007/978-3-642-69320-5.

28. C. Dickson, D. Brew, and F. Glasser, "Solubilities of $CaO–SiO_2–H_2O$ Phases at 25, 55 and 85 C," *Advances in Cement Research* 16 (2004): 35–43, https://doi.org/10.1680/adcr.2004.16.1.35.

29. C. DIckson, D. Brew, and F. Glasser, *Solubilities of Crystalline Calcium Silicate Hydrates* (University of Aberdeen, 2002).

30. P. Blanc, P. Piantone, A. Lassin, and A. Burnol, Thermochimie: Sélection de constantes thermodynamiques pour les éléments majeurs, le plomb et le cadmium, Final report: BRGM RP-54902-FR (2006).

31. L. Glasser and H. D. B. Jenkins, "Predictive Thermodynamics for Ionic Solids and Liquids," *Physical Chemistry Chemical Physics* 18 (2016): 21226–21240, https://doi.org/10.1039/C6CP00235H.

32. K. Baltakys and T. Dambrauskas, *Synthesis and Properties of Gyrolite, Synthetic Gyrolite: A Dual Solution for Wastewater Treatment and Portland Cement* (Springer Nature, 2024), 41–77.

33. J. Meyer and K. Jaunarajs, "Synthesis and Crystal Chemistry of Gyrolite and Reyerite," *American Mineralogist: Journal of Earth and Planetary Materials* 46 (1961): 913–933.

34. S. Shaw, C. M. B. Henderson, and S. M. Clark, "In-Situ Synchrotron Study of the Kinetics, Thermodynamics, and Reaction Mechanisms of the Hydrothermal Crystallization of Gyrolite, $Ca_{16}Si_{24}O_{60}(OH)_8{\cdot}14H_2O$," *American Mineralogist* 87 (2002): 533–541, https://doi.org/10.2138/am-2002-0416.

35. R. Siauciunas and K. Baltakys, "Formation of Gyrolite During Hydrothermal Synthesis in the Mixtures of CaO and Amorphous SiO_2 or Quartz," *Cement and Concrete Research* 34 (2004): 2029–2036, https://doi.org/10.1016/j.cemconres.2004.03.009.

36. J. Gard, T. Mitsuda, and H. Taylor, "Some Observations on Assarsson's Z-Phase and Its Structural Relations to Gyrolite, Truscottite, and Reyerite," *Mineralogical Magazine* 40 (1975): 325–333, https://doi.org/10.1180/minmag.1975.040.312.01.

37. T. Mitsuda, J. Saito, and E. Hattori, "Influence of Starting Materials on the Hydrothermal Formation of Xonotlite at 180 C," in *Proceedings of the 1st International Symposium on Hydrothermal Reactions Held March 22–26, 1982 in Japan*, ed. S. Somiya, (Association for Science Documents Information, 1983), 823–838.

38. B. Lothenbach, D. Jansen, Y. Yan, and J. Schreiner, "Solubility and Characterization of Synthesized 11 Å Al-Tobermorite," *Cement and Concrete Research* 159 (2022): 106871, https://doi.org/10.1016/j.cemconres.2022.106871.

39. T. Mitsuda, "Paragenesis of 11 Å Tobermorite and Poorly Crystalline Hydrated Magnesium Silicate," *Cement and Concrete Research* 3 (1973): 71–80, https://doi.org/10.1016/0008-8846(73)90062-8.

40. K. Schmeide, N. M. Huittinen, S. S. A. Azzam, et al., "Uranium (VI) Retention by Calcium (Alumino) Silicate Hydrates–Impact of Temperature and Ionic Strength," *Applied Geochemistry* 186 (2025): 106400, https://doi.org/10.1016/j.apgeochem.2025.106400.

41. S. Mingione, D. Jansen, F. Winnefeld, S. Churakov, and B. Lothenbach, "Effect of Mg on Xonotlite Structure and Stability," *Cement and Concrete Research* 197 (2025): 107970, https://doi.org/10.1016/j.cemconres.2025.107970.

42. K. Baltakys and R. Siauciunas, "The Influence of γ-Al_2 O_3 and Na_2O on the Formation of Gyrolite in the Stirring Suspension," *Journal of Materials Science* 41 (2006): 4799–4805, https://doi.org/10.1007/s10853-006-0049-0.

43. A. Bankauskaite, A. Eisinas, K. Baltakys, and S. Zadaviciute, "A Study on the Intercalation of Heavy Metal Ions in a Wastewater by Synthetic Layered Inorganic Adsorbents," *Desalination and Water Treatment* 56 (2015): 1576–1586, https://doi.org/10.1080/19443994.2014.951074.

44. E. Bobinaite, S. Mingione, B. Lothenbach, and T. Dambrauskas, "Influence of Fe3+ Ions on the Formation of Gyrolite" manuscript submitted to Journal of Thermal Analysis and Calorimetry (2026)- Still under review.

45. B. Z. Dilnesa, B. Lothenbach, G. Renaudin, A. Wichser, and D. Kulik, "Synthesis and Characterization of Hydrogarnet Ca_3 $(AlxFe_{1-x})_2$ $(SiO_4)_y$ $(OH)_{4(3-y)}$," *Cement and Concrete Research* 59 (2014): 96–111, https://doi.org/10.1016/j.cemconres.2014.02.001.

46. D. Jansen, C. Stabler, F. Goetz-Neunhoeffer, S. Dittrich, and J. Neubauer, "Does Ordinary Portland Cement Contain Amorphous Phase? A Quantitative Study Using an External Standard Method," *Powder Diffraction* 26 (2011): 31–38.

47. T. Armbruster, "Structure Refinement of Hydrous Andradite, $Ca_3Fe_{1.54}Mn_{0.26}(SiO4)_{1.65}(O_4H_4)_{1.35}$, From the Wessels Mine, Kalahari Manganese Field, South Africa," *European Journal of Mineralogy* 7 (1995): 1221–1226, https://doi.org/10.1127/ejm/7/5/1221.

48. S. A. Markgraf and R. J. Reeder, "High-Temperature Structure Refinements of Calcite and Magnesite," *American Mineralogist* 70 (1985): 590–600.

49. V. Streltsov, V. Tsirelson, R. Ozerov, and O. Golovanov, "Electronic and Thermal Parameters of Ions in CaF_2 as a Result of Application of the Regularized Least-Squares Method," *Kristallografiya* 33 (1988): 90–97.

50. D. Ectors, F. Goetz-Neunhoeffer, and J. Neubauer, "A Generalized Geometric Approach to Anisotropic Peak Broadening due to Domain Morphology," *Applied Crystallography* 48 (2015): 189–194, https://doi.org/10.1107/S1600576714026557.

51. C. Hejny and T. Armbruster, "Polytypism in Xonotlite $Ca_6Si_6O_{17}$ $(OH)_2$," *Zeitschrift für Kristallographie-Crystalline Materials* 216 (2001): 396–408, https://doi.org/10.1524/zkri.216.7.396.20363.

52. S. Mingione, D. Jansen, F. Winnefeld, S. Churakov, and B. Lothenbach, "Effect of Temperature on the Solubility of Xonotlite," *Cement and Concrete Research* 188 (2025): 107732, https://doi.org/10.1016/j.cemconres.2024.107732.

53. T. Wagner, D. A. Kulik, F. F. Hingerl, and S. V. Dmytrieva, "GEM-Selektor Geochemical Modeling Package: TSolMod Library and Data Interface for Multicomponent Phase Models," *Canadian Mineralogist* 50 (2012): 1173–1195, https://doi.org/10.3749/canmin.50.5.1173.

54. D. A. Kulik, T. Wagner, S. V. Dmytrieva, et al., "GEM-Selektor Geochemical Modeling Package: Revised Algorithm and GEMS3K Numerical Kernel for Coupled Simulation Codes," *Computational Geosciences* 17 (2013): 1–24.

55. T. Thoenen, W. Hummel, U. Berner, and E. Curti, The PSI/Nagra Chemical Thermodynamic Database 12/07, PSI Bericht No. 14-04 (Paul Scherrer Institut, 2014).

56. B. Lothenbach, D. A. Kulik, T. Matschei, et al., "Cemdata18: A Chemical Thermodynamic Database for Hydrated Portland Cements and Alkali-Activated Materials," *Cement and Concrete Research* 115 (2019): 472–506, https://doi.org/10.1016/j.cemconres.2018.04.018.

57. D. A. Kulik, G. D. Miron, and B. Lothenbach, "A Structurally-Consistent CASH+ Sublattice Solid Solution Model for Fully Hydrated CSH Phases: Thermodynamic Basis, Methods, and Ca-Si-H_2O Core Sub-Model," *Cement and Concrete Research* 151 (2022): 106585, https://doi.org/10.1016/j.cemconres.2021.106585.

58. H. C. Helgeson, D. H. Kirkham, and G. C. Flowers, "Theoretical Prediction of the Thermodynamic Behavior of Aqueous Electrolytes by High Pressures and Temperatures; IV, Calculation of Activity Coefficients, Osmotic Coefficients, and Apparent Molal and Standard and Relative Partial Molal Properties to 600 Degrees C and 5Kb," *American journal of science* 281 (1981): 1249–1516.

59. G. M. Anderson and D. A. Crerar, Thermodynamics in Geochemistry: The Equilibrium Model (Oxford University Press, 1993).

60. W. Hummel and T. Thoenen, The PSI Chemical Thermodynamic Database 2020, Technical Report 21-03 (Paul Scherrer Institut, 2023), 1411.

61. C. A. Geiger, E. Dachs, N. M. Vielreicher, and G. R. Rossman, "Heat Capacity and Entropy Behavior of andradite: A Multi-Sample and -Methodological Investigation," *European Journal of Mineralogy* 30 (2018): 681–694, https://doi.org/10.1127/ejm/2018/0030-2741.

62. E. Dachs and C. A. Geiger, "Thermodynamic Behaviour of Grossular–Andradite, Ca_3 $(Al_x$ $Fe^{3+}{}_{1\text{-}x}$ $)_2Si_3O_{12}$, Garnets: A Calorimetric Study," *European Journal of Mineralogy* 31 (2019): 443–451, https://doi.org/10.1127/ejm/2019/0031-2827.

63. Y. Okada, T. Masuda, M. Takada, L. Xu, and T. Mitsuda, *Relationship Between NMR 29 Si Chemical Shifts and FT-IR Wave Numbers in Calcium Silicates, Nuclear Magnetic Resonance Spectroscopy of Cement-Based Materials* (Springer-Verlag Berlin, 1998), 69–78.

64. K. Garbev, "Structure, Properties and Quantitative Rietveld Analysis of Calcium Silicate Hydrates (CSH-Phases) " (PhD diss., Ruprecht-Karls-Universität Heidelberg, 2004).

65. K. Baltakys and R. Siauciunas, "Physically and Chemically Bound H_2O in the Gyrolite Structure," *Materials Science Poland* 27 (2009): 255–263.

66. L. Dent and H. Taylor, "The Dehydration of Xonotlite," *Acta Crystallographica* 9 (1956): 1002–1004, https://doi.org/10.1107/S0365110X56002916.

67. S. Haastrup, D. Yu, and Y. Yue, "Impact of minor Iron Content on Crystal Structure and Properties of Porous Calcium Silicates During Synthesis," *Materials Chemistry and Physics* 205 (2018): 180–185, https://doi.org/10.1016/j.matchemphys.2017.11.024.

68. N. Mostafa, E. Kishar, and S. Abo-El-Enein, "FTIR Study and Cation Exchange Capacity of Fe^{3+}- and Mg^{2+}-Substituted Calcium Silicate Hydrates," *Journal of alloys and compounds* 473 (2009): 538–542, https://doi.org/10.1016/j.jallcom.2008.06.029.

69. O. Ferro, E. Galli, G. Papp, S. Quartieri, S. Szakáll, and G. Vezzalini, "A New Occurrence of Katoite and Re-Examination of the Hydrogrossular Group," *European Journal of Mineralogy* 15 (2003): 419–426, https://doi.org/10.1127/0935-1221/2003/0015-0419.

70. G. Amthauer and G. R. Rossman, "The Hydrous Component in Andradite Garnet," *American Mineralogist* 83 (1998): 835–840, https://doi.org/10.2138/am-1998-7-815.

71. E. Bernard, B. Lothenbach, D. Rentsch, I. Pochard, and A. Dauzères, "Formation of Magnesium Silicate Hydrates (MSH), Physics and Chemistry of the Earth," *Parts A/B/C* 99 (2017): 142–157, https://doi.org/10.1016/j.pce.2017.02.005.

72. R. Levinskas, A. Baltušnikas, I. Lukošiūtė, K. Baltakys, R. Kalpokaitė-Dičkuvienė, and A. Grybėnas, "Modification of Structure of Synthetic Gyrolite," *Materials Research Innovations* 17 (2013): 495–500, https://doi.org/10.1179/1433075X13Y.0000000103.

73. J. Yajun and J. H. Cahyadi, "Effects of Densified Silica Fume on Microstructure and Compressive Strength of Blended Cement Pastes," *Cement and concrete research* 33 (2003): 1543–1548, https://doi.org/10.1016/S0008-8846(03)00100-5.

74. E. Bernard, M. Yio, D. Rentsch, H. Chen, and R. J. Myers, “Insights on the Effects of Carbonates and Phosphates on the Hydration of Magnesia (alumino-) Silicate Cements,” *Applied Geochemistry* 167 (2024): 106001, https://doi.org/10.1016/j.apgeochem.2024.106001.

75. H. Maeda, Y. Kurosaki, T. Nakamura, M. Nakayama, E. H. Ishida, and T. Kasuga, “Control of Chemical Composition of Hydrogrossular Prepared by Hydrothermal Reaction,” *Materials Letters* 131 (2014): 132–134, https://doi.org/10.1016/j.matlet.2014.05.168.

76. E. Passaglia and R. Rinaldi, “Katoite, a New Member of the Ca3Al2 (SiO4) 3-Ca3Al2 (OH) 12 Series and a New Nomenclature for the Hydrogrossular Group of Minerals,” *Bulletin de Minéralogie* 107 (1984): 605–618, https://doi.org/10.3406/bulmi.1984.7804.

77. J. Liu, X. Pan, H. Wu, F. Qiu, and H. Yu, “Effect of Iron Minerals on Formation of Hydroandradite During Alkali-thermal Process,” *Journal of Industrial and Engineering Chemistry* 142 (2025): 676–685, https://doi.org/10.1016/j.jiec.2024.08.010.

78. D. Hou, W. Zhang, J. Sun, and J. Zhang, “Structure, Dynamics and Mechanical Properties Evolution of Calcium-silicate-hydrate Induced by Fe Ions: A Molecular Dynamics Study,” *Construction and Building Materials* 287 (2021): 122875, https://doi.org/10.1016/j.conbuildmat.2021.122875.

79. G. Ovcharenko, E. Ibe, and A. Viktorov, “Assessment of the Influence of Additives in Concrete by the Raman Spectroscopy Method,” in *E3S Web of Conferences* (EDP Sciences, 2020), 06004.

80. A. Mancini, E. Wieland, G. Geng, et al., “Fe (III) Uptake by Calcium Silicate Hydrates,” *Applied Geochemistry* 113 (2020): 104460, https://doi.org/10.1016/j.apgeochem.2019.104460.

81. Y. Fang, K. Zhuang, H. Cui, et al., “The state of Fe^{3+} in the C–F–A–S–H System With Varying Fe/Si and Ca/Si Ratios,” *Journal of Materials Chemistry A* 11 (2023): 26193–26211, https://doi.org/10.1039/D3TA01929B.

82. S. V. Churakov and P. Mandaliev, “Structure of the Hydrogen Bonds and Silica Defects in the Tetrahedral Double Chain of Xonotlite,” *Cement and Concrete Research* 38 (2008): 300–311, https://doi.org/10.1016/j.cemconres.2007.09.014.

83. Q. Wang, J. P. Zhang, T. R. Smith, W. E. Hurst, and T. Sulpizio, “An Electrokinetic Study on a Synthetic Adsorbent of Crystalline Calcium Silicate Hydrate and Its Mechanism of Endotoxin Removal,” *Colloids and Surfaces B: Biointerfaces* 44 (2005): 110–116, https://doi.org/10.1016/j.colsurfb.2005.06.005.

84. D. A. Kulik, “Improving the Structural Consistency of CSH Solid Solution Thermodynamic Models,” *Cement and Concrete Research* 41 (2011): 477–495, https://doi.org/10.1016/j.cemconres.2011.01.012.

85. G. Smalakys and R. Siauciunas, “Peculiarities of Xonotlite Synthesis From the Raw Materials With Different SiO_2 Activities,” *Journal of Thermal Analysis and Calorimetry* 142 (2020): 1671–1679, https://doi.org/10.1007/s10973-020-09744-2.

86. L. N. Warr, “IMA–CNMNC Approved Mineral Symbols,” *Mineralogical Magazine* 85 (2021): 291–320, https://doi.org/10.1180/mgm.2021.43.

87. J. Zoldi, K. Solymar, J. Zambo, and K. Jonas, “Iron Hydrogarnets in the Bayer Process,” in *Proceedings of TMS Light Metals* (The Minerals, Metals & Materials Society, 1987), 105–111.

88. X. Li, S. Gu, Z. Yin, G. Wu, and Y. Zhai, “Regulating the Digestion of High Silica Bauxite With Calcium Ferrite Addition,” *Hydrometallurgy* 104 (2010): 313–316, https://doi.org/10.1016/j.hydromet.2010.06.008.

89. X. Pan, H. Wu, J. Liu, Q. Liu, and H. Yu, “Hydrothermal Formation Mechanism of the Efficient Desilication Product Hydroandradite ($3CaO{\cdot}Fe_2O3{\cdot}_xSiO_2{\cdot}(6\text{-}2_x)\ H_2O$),” *Hydrometallurgy* 203 (2021): 105695, https://doi.org/10.1016/j.hydromet.2021.105695.

Supporting Information

Additional supporting information can be found online in the Supporting Information section.

Supporting File 1: jace70634-sup-0001-SuppMat.docx.